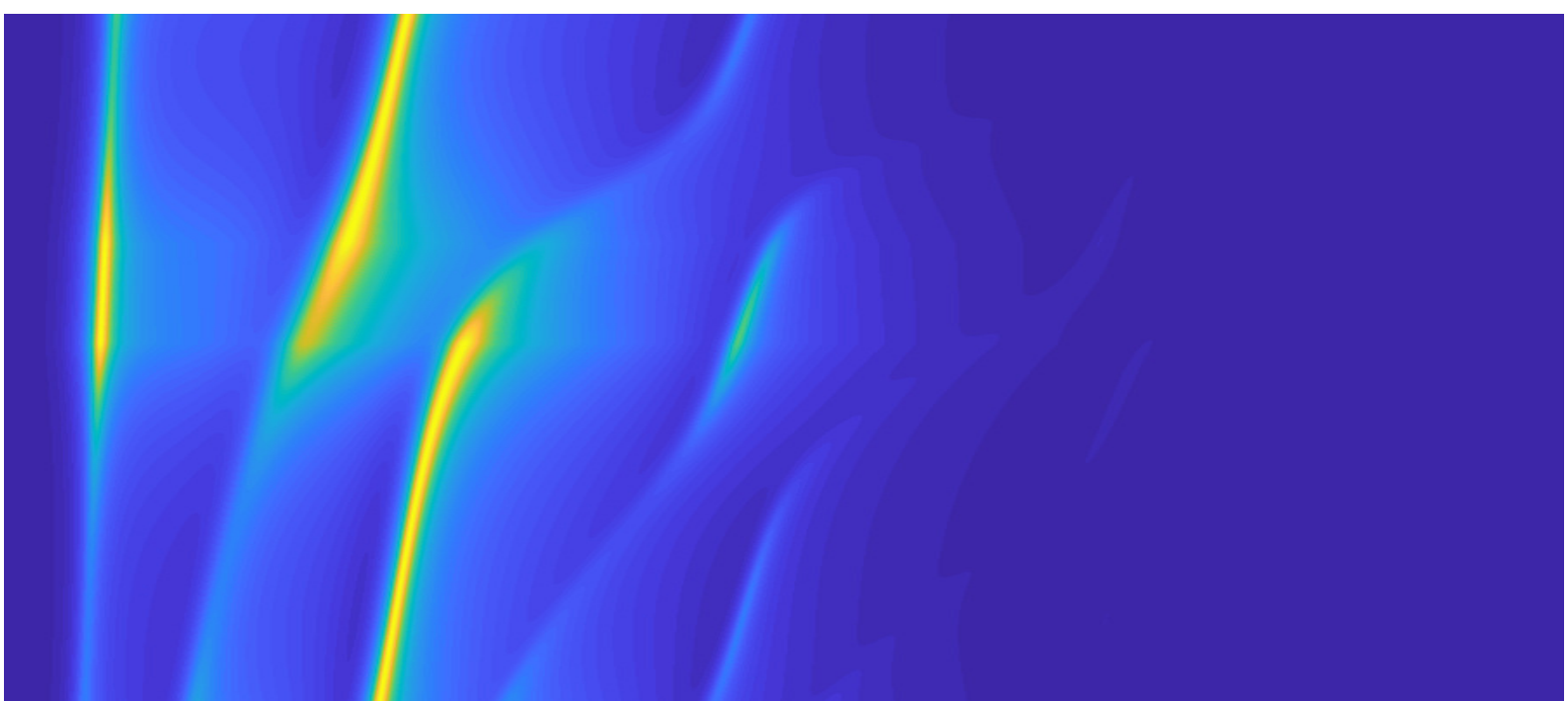


Inversion Scheme for Multichannel Impact Echo Measurements

Adriaan W.M. Imhoff

Master's Thesis
Computational Imaging
Delft University of Technology



Inversion Scheme for Multichannel Impact Echo Measurements

by

Adriaan W.M. Imhoff

to obtain the degree of Master of Science in Applied Physics
at the Delft University of Technology,
to be defended publicly on Thursday February 20th, 2020 at 10:00.

Student number: 4374479
Project duration: February 1, 2019 - February 20, 2020
Supervisors: Dr. D.J. Verschuur Computational Imaging, TU Delft
Dr. K.W.A. van Dongen Medical Imaging, TU Delft
Thesis committee: Prof. N. de Jong Medical Imaging, TU Delft & Erasmus MC
Dr. D.J. Verschuur Computational Imaging, TU Delft
Dr. A.J.L. Adam Optics, TU Delft
Ir. G.M. Louwerse Extern, TATA Steel

An electronic version of this thesis is available at <http://repository.tudelft.nl/>.



Summary

Conventional imaging techniques from medical ultrasound and seismic imaging are not suitable for multi-layered domains where there is no separation between received reflection events. This happens in layered structures where the thickness of the individual layer is small with respect to the induced wavelengths. An example of these structures is the wall of a typical blast furnace. Imaging these domains require a method based on the interference pattern in the frequency domain. This method is already widely used for imaging concrete structures. However, these consists of only one or two layers. This study introduces a Full Waveform Inversion scheme which extends the usability of the method to multilayered domains. It minimizes the error between measurements and a forward model. To reduce the computation load, a simplified forward model based on a plane wave response in a vertically layered medium is adopted. Pre-processing steps are necessary to remove the effect of the source wavelet and to enhance the peaks and troughs positions. A sensitivity analysis provides information about the usability of the method. This shows only layers with standing wave frequencies in the range of the induced source wavelet can be imaged. Furthermore, results show it is impossible to measure the wave velocity and thickness of a single layer simultaneously given our simplified forward model. Multichannel measurements over an aperture of 500 mm are required to transform a spherical wave response to its plane wave equivalent in order to fit the forward model. Tapering the sides of the aperture is essential to reduce simulation artefacts. The inversion scheme is successfully tested on synthetic data of a blast furnace wall in the acoustic and elastic domain using realistic simulations of the measured data.

Contents

List of Figures	vii
List of Tables	ix
1 Introduction	1
1.1 Applications	2
1.1.1 Thermocouples	2
1.1.2 Infrared-thermography	2
1.1.3 Radioactive tracers.	2
1.1.4 Electromagnetic techniques	3
1.1.5 Core drilling	3
1.2 Research aim and outline	3
2 Theory	5
2.1 Wave propagation.	5
2.1.1 Acoustic media.	5
2.1.2 Elastic media.	6
2.1.3 Reflection and Transmission.	6
2.2 Standing wave theory	7
2.3 Multichannel measurements	8
3 Modelling	11
3.1 Elastic Finite Difference model	11
3.1.1 Convergence and stability criteria	12
3.1.2 Boundary conditions.	13
3.2 Wavefield Modelling via Bremmer Serie.	13
4 Inversion	15
4.1 Inversion Scheme 1: Single peak inversion	15
4.2 Inversion Scheme 2: Minimizing an objective function	15
5 Results	19
5.1 Sensitivity analysis	20
5.1.1 Density	20
5.1.2 Wave velocity	21
5.1.3 Thickness	21
5.2 Inversion	21
5.2.1 Single peak inversion	21
5.2.2 Minimizing an objective function	22
5.3 Multichannel measurements	24
6 Discussion, Recommendations, and Conclusions	29
6.1 Discussion and Recommendation	29
6.1.1 Modelling	29
6.1.2 Sensitivity analysis	29
6.1.3 Inversion.	29
6.1.4 Multichannel measurements.	30
6.2 Conclusion	30

A	Fourier Transform	31
B	Derivation Angle-Dependent Transmission and Reflection Coefficients	33
C	Kenneth Modelling	35
D	Inversion Data	37
	D.1 Varying frequency window	37
	D.2 Varying scaling factor	40
	Bibliography	43
	Acknowledgements	45

List of Figures

1.1	A typical A-scan of a signal with no separated arrivals in the (a) time domain and (b) frequency domain.	1
1.2	Schematic cross section of the inside lining of a furnace wall with: (1) air, (2) steel shell, (3) mortar joint, (4) graphite, (5) ramming layer, (6) semi-graphite blocks, and (7) liquid steel.	2
2.1	Resonance frequency visualized for the first three harmonics. Top $n = 1$, centre $n = 2$, bottom $n = 3$ taken for two positive reflection coefficients (left), one negative reflection coefficient on the left side of the domain (middle), and two negative reflection coefficients (right).	7
2.2	Example of a recorded wavefield of a domain with one reflective boundary. (S1) 1th Fresnel zone ,(S2) wavefield at the boundary, (S3) the remaining wavefield.	9
3.1	Staggered grid for updating the particles velocity \dot{u}_x and \dot{u}_z (Thorbecke and Draganov, 2011).	12
3.2	Staggered grid for updating the pressure P (Thorbecke and Draganov, 2011).	12
3.3	Suppression factor β for taper factor α between 0 (blue) and 2 (green) in increments of 0.1 over 50 grid points.	13
4.1	Block diagram for minimizing the objective function.	16
4.2	Compression function for different scaling factors γ between 0 (blue) and 5 (green) in increments of 0.5. Δ is the normalized difference between the absolute spectrum and its moving mean.	16
4.3	Example of a frequency spectra with and without pre-processing steps. (a) the absolute spectrum (solid) and the moving mean (dashed). (b) normalized difference between the absolute spectrum and its moving mean, Δ , without (dashed) and with compression function (solid). Here the moving mean is created with a window size of 750 Hz, γ equals 3.	17
5.1	Source wavelet used in the experiment: Ricker wavelet with $dt=1e-4$ ms, $nt=7000$, a peak frequency of 3 kHz and a maximum frequency of 10 kHz in (a) the time domain and (b) as absolute frequency spectra.	20
5.2	Absolute frequency spectra for varying densities between 70 and 130 percent of the design specification. (a) steel shell, (b) mortar joint, (c) graphite, (d) ramming layer, and (e) semi-graphite. All spectra are made with sFWMod.	20
5.3	Absolute frequency spectra for varying wave velocities between 70 and 130 percent of the design specification. (a) steel shell, (b) mortar joint, (c) graphite, (d) ramming layer, and (e) semi-graphite. All spectra are made with sFWMod.	21
5.4	Absolute frequency spectra for varying thicknesses between 70 and 130 percent of the design specification. (a) steel shell, (b) mortar joint, (c) graphite, (d) ramming layer, and (e) semi-graphite. All spectra are made with sFWMod.	22
5.5	(a) absolute frequency spectra for varying semi-graphite thickness between 0 and 750 mm (made with sFWMod). The rectangle box indicates the region of interest for creating the function. (b) peak position versus semi-graphite thickness with the straight line being the fit.	22
5.6	Example received frequency spectra for <code>fde1modc</code> (red) and <code>sFWMod</code> (blue) with (a) no pre-processing steps, and (b) with pre-processing steps (frequency window of 750 Hz, γ equals 3).	23
5.7	Error surfaces for varying graphite and semi-graphite thicknesses The dot represents the input parameters in <code>fde1modc</code> . (a) no pre-processing, (b) applied pre-processing (window size of 700 Hz, γ equals 3).	23
5.8	Error surfaces using various window sizes from (a) 300 Hz to (e) 2300 Hz in steps of 500 Hz.	24
5.9	Received signal of multichannel measurements in the acoustic domain. Plane wave source in (a) the time domain and (b) the frequency domain. Point source in (a) the time domain and (b) the frequency domain.	26

5.10	Received signal of multichannel measurements in the elastic domain. Plane wave source in (a) the time domain and (b) the frequency domain. Point source in (a) the time domain and (b) the frequency domain.	26
5.11	Normalized frequency responses for the acoustic domain. sFWMod (orange), plane wave response created with <code>fdelmodc</code> (red), spherical wave response (blue) for a spatial window of (a) 5000 mm with no tapering, and Tukey apertures of (b) 500 mm, (c) 1000 mm, and (d) 1500 mm with a cosine fraction of 0.6.	27
5.12	Normalized frequency responses for the elastic domain. sFWMod (orange), plane wave response created with <code>fdelmodc</code> (red), spherical wave response (blue) for a spatial window of (a) 5000 mm with no tapering, and Tukey apertures of (b) 500 mm, (c) 1000 mm, and (d) 1500 mm with a cosine fraction of 0.6.	27
D.1	Error plots for 200 parameter sets \mathbf{m} with varying frequency windows for calculating the moving mean of (a) 750 to (f) 2000 Hz.	37
D.2	Histograms for entire parameter set $\{\mathbf{m}\}$. Different frequency windows for calculating the moving mean of (a) 750 to (f) 2000 Hz in increments of 250 Hz. x.1, x.2, x.3, x.4 show the histogram for the errors, and graphite, ramming, and semi-graphite layer thickness, respectively.	38
D.3	Histograms for 50 parameter \mathbf{m} with lowest error. Different frequency windows for calculating the moving mean of (a) 750 to (f) 2000 Hz in increments of 250 Hz. x.1, x.2, x.3, x.4 show the histogram for the errors, and graphite, ramming, and semi-graphite layer thickness, respectively.	39
D.4	Error plots for 200 parameter sets \mathbf{m} with varying compression functions with scaling factors γ of (a) 1 to (f) 6.	40
D.5	Histograms for entire parameter set $\{\mathbf{m}\}$. Different compression functions with scaling factors γ between (a) 1 to (f) 6 in increments of 1 Hz. x.1, x.2, x.3, x.4 show the histogram for the errors, and graphite, ramming, and semi-graphite layer thickness, respectively.	41
D.6	Histograms for 50 parameter \mathbf{m} with lowest error. Different compression functions with scaling factors γ between (a) 1 to (f) 6 in increments of 1 Hz. x.1, x.2, x.3, x.4 show the histogram for the errors, and graphite, ramming, and semi-graphite layer thickness, respectively.	42

List of Tables

3.1	Schematic view of the wavefields \hat{P} and \hat{Q} , reflection R and transmission T, and propagation operators \hat{W}	13
3.2	Symbols in the sFWMod scheme.	13
5.1	Properties of the different layers in the refractory and liquid steel. Here the subscript p and s denote the acoustic and elastic properties, respectively. ¹ Thicknesses according to design. ² Wave velocities are set to be constant, while in fact these are not due to a temperature gradient. The reflection and transmission coefficients are valid for plane waves at normal incidence only and are defined as in Fig. 3.1.	19
5.2	Statistics of the best 20 parameter sets with lowest error for different frequency window sizes. d_3 , d_4 , and d_5 represent the thickness of the graphite, ramming layer, and semi-graphite layer, respectively. A compression function with a scaling factor γ of 3 is used.	24
5.3	Statistics of the best 20 parameter sets with lowest error for different scaling factors γ in the compression function. d_3 , d_4 , and d_5 represent the thickness of the graphite, ramming layer, and semi-graphite layer, respectively. A frequency window size of 1000 Hz is used.	25
5.4	Statistics of the best 20 parameter sets with lowest error for different aperture widths for a point source in the acoustic domain. d_3 , d_4 , and d_5 represent the thickness of the graphite, ramming layer, and semi-graphite layer, respectively. A frequency window size of 1000 Hz and a scaling factor of 3 is used.	25

Introduction

Sound waves are widely used for imaging. High frequencies are required to image small domains. Medical ultrasound is such an example where acoustic waves with frequencies of multiple megahertz are used. Larger domains, such as in geophysics, require longer wavelengths to counteract absorption of the media. In both fields the arrivals are separated in time. This makes it possible to use traditional imaging and inversion techniques. These methods, however, do not suffice when there is no clear distinction between arrivals. This phenomena occurs mostly in imaging layers smaller than the induced wavelength. For multilayered domains this effect becomes even more apparent. Here an imaging technique called Impact-Echo (IE) can be used. It uses an impact device, normally a hammer, to induce a wave. The received signal is Fourier transformed and the frequency spectrum contains information about the system parameters. Fig. 1.1a shows a typical signal of one receiver. There is no distinction between arriving waves. However, when this signal is Fourier transformed, see Fig. 1.1b, more information is visible. This method has been the standard for imaging concrete structures for several decades (Theocaris and Prassianakis, 1974; John et al., 1982). However, these structures are limited to only one or two layers such that the resonance frequency can be easily determined. This study introduces an inversion scheme for imaging multilayered domains using the IE method and multichannel data.

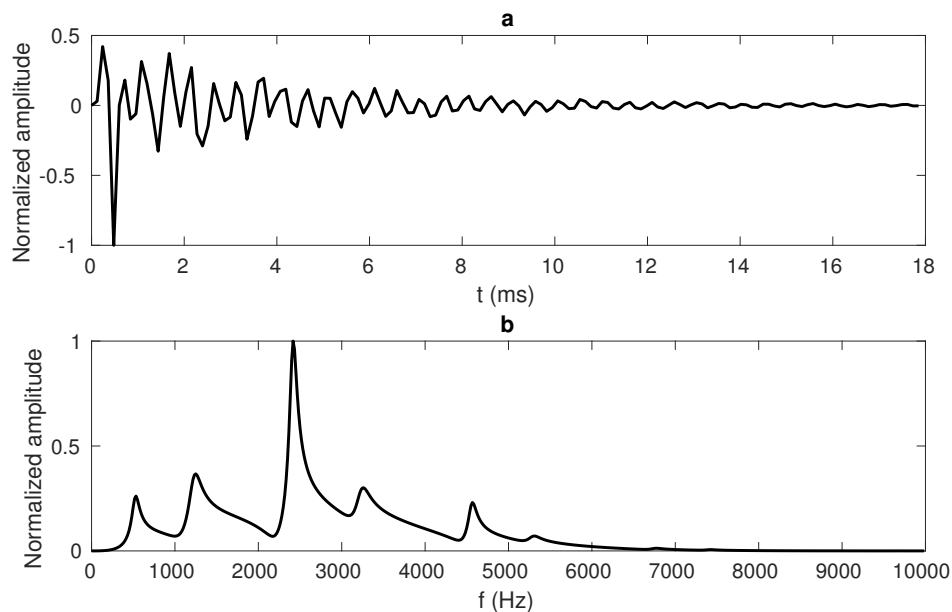


Figure 1.1: A typical A-scan of a signal with no separated arrivals in the (a) time domain and (b) frequency domain.

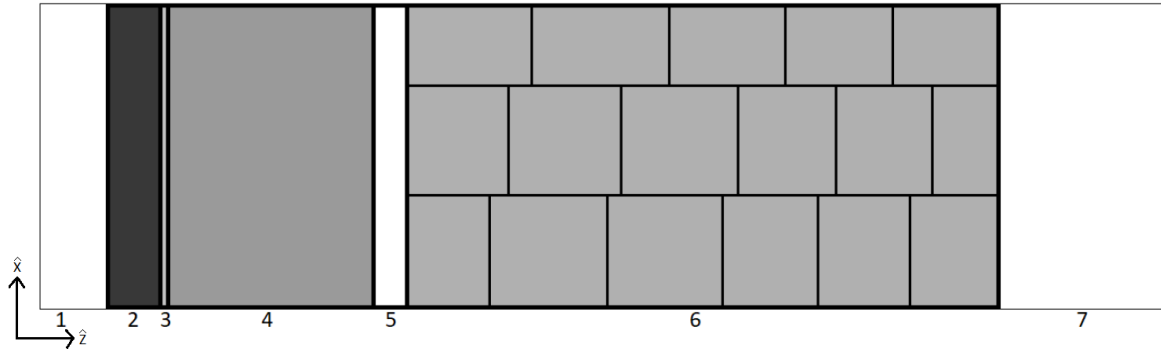


Figure 1.2: Schematic cross section of the inside lining of a furnace wall with: (1) air, (2) steel shell, (3) mortar joint, (4) graphite, (5) ramming layer, (6) semi-graphite blocks, and (7) liquid steel.

1.1. Applications

The proposed inversion scheme can be used for various multilayered systems with layers thinner than the induced wavelengths. In this study the inversion scheme is tested on simulated measurements of the hearth of a typical blast furnace. This hearth is cylindrically shaped with a diameter of 13 meter and a height of almost 9 meter. Its wall, called the refractory, consists of five different layers with a design thickness varying between 2 and 750 millimetre, see Fig 1.2 for a schematic cross-section. There is a need for imaging the refractory as it degrades over time. Especially the semi-graphite blocks (layer 6 in Fig. 1.2) experience a high level of degradation. This is mainly caused by high temperature molten corrosion, thermal shock, and carbon brig fragmentation (Wang et al., 2014; Sadri et al., 2015). Monitoring the degradation will increase the overall safety and maintenance scheduling (Sadri et al., 2014). Moreover, the lifespan of the furnace can be increased up to 15 percent when imaging the refractory with an accurate technique.

Currently there exist several imaging methods for this application. However, these all have their own disadvantages and limitations. The top five most used methods are given in the following subsections.

1.1.1. Thermocouples

This is, together with infrared-thermography, the most common monitoring technique. It uses the temperature values and a mathematical model to determine the thickness. The temperature values are obtained via thermocouples at specific positions inside the wall. This method seems sufficient, however, assumptions and predictability strongly influence the accuracy. When the medium is assumed to be homogeneous, while in fact this is never the case, significant errors will arise. Furthermore, the accuracy of the temperature data is limited. This will have a significant effect on the thickness determination (Sadri et al., 2015; Sharp et al., 2012).

1.1.2. Infrared-thermography

Infrared-thermography uses an infrared camera to detect hot spots on the steel shell. Weak parts of the wall can be determined using these hot spots. This method has some drawbacks. Cracks, gaps and looseness of the bonding will affect the result dramatically. Additionally, these rough estimates need to be compared to earlier data sets. This requires similar measurement conditions. Also, rusting, nearby heat, and reflections will affect the temperature reading (Sadri et al., 2015; Bolf, 2004; Sadri et al., 2009).

1.1.3. Radioactive tracers

Radioactive tracers are inserted through the top of the furnace, after which the descent and radiate through the wall. The radioactive intensity measured outside the furnace is proportional to the remaining thickness. However, non uniformity of the layers, the presence of molten metal throughout the layers, and quality of the remaining lining will result in inconsistent radiation counts. Furthermore, the tracers can be toxic which might lead to health risks for operators (Sadri et al., 2015).

1.1.4. Electromagnetic techniques

Radar and microwave systems are used to measure spatial variations in the dielectric constants. These variations can be linked to the remaining thickness (Varghese et al., 2005). Because it is impossible for electromagnetic waves to penetrate the steel shell, antennas need to be placed inside the furnace wall. However, any other steel in the lining – which will occur either by design or by deterioration – will result in interference or completely block the signal. It is also impossible to detect empty voids as electromagnetic waves are insensitive to refractory-air interfaces (Sadri et al., 2015).

1.1.5. Core drilling

Core drilling is the most accurate technique. Here a core is drilled up to a pre-determined temperature depth. Within this core the remaining thickness can be determined. However, the use of this technique is limited as it affects the structure and safety of the furnace. Furthermore, this method results in a local profile only.

1.2. Research aim and outline

Due to the various limitations of the above described technique, there is a need for a more safe and robust imaging method. The aim of this study is to test the feasibility of an interference pattern based inversion scheme as imaging technique. This is tested for both plane wave and point sources in acoustic and elastic media. Due to the preliminary nature of this study, only vertical profile geometries are considered. This entails no local degradation or tilted boundaries. The proposed inversion scheme is tested on synthetic data of a refractory only. Multichannel measurements are used to transform the response of a point source to its plane wave equivalent.

The outline of this thesis is as follows. First, wave propagation in both acoustic and elastic media is described. This chapter also encloses the standing wave theory and the theory of multichannel measurements. The next chapter introduces two modelling methods. Chapter 4 explores two inversion schemes. Chapter 5 encloses the results. Here a sensitivity analysis is performed, and the inversion methods are tested on synthetic data. Furthermore, data of multichannel measurements is explored. Lastly the conclusion and recommendations are given.

2

Theory

This chapter introduces the necessary theory of both acoustic and elastic wave propagation. Next, reflection and transmission at boundaries is explained and the standing wave theory is explored for both single and multilayered domains. Lastly, Fourier theory regarding multichannel measurements is introduced.

2.1. Wave propagation

Sound waves can propagate in two different kinds of media: acoustic media and elastic media. Acoustic media have zero shear modulus while elastic media do not. This result in two different types of wave equations. Acoustic waves obey to a scalar equation while elastic waves adhere to a vectorized equation.

2.1.1. Acoustic media

The acoustic wave equation can be derived from Hooke's law,

$$-\nabla \cdot \mathbf{u}(\mathbf{r}, t) = -\frac{p(\mathbf{r}, t)}{\kappa(\mathbf{r})} + q(\mathbf{r}, t), \quad (2.1)$$

and Newton's law,

$$\mathbf{f}(\mathbf{r}, t) - \nabla p(\mathbf{r}, t) = \rho(\mathbf{r}) \frac{\delta \mathbf{v}(\mathbf{r}, t)}{\delta t}. \quad (2.2)$$

Here \mathbf{u} [m], \mathbf{v} [m s⁻¹] and p [Pa] represent the particle position, particle velocity and the pressure, respectively. κ [Pa⁻¹] is the bulk modulus and ρ [kg m⁻³] is the density. Sources, when present, are given by q [-] and \mathbf{f} [N m⁻³]. These are the volume injected per unit volume and force per unit volume, respectively. Note that the bold symbols refer to vectorized quantities. The acoustic wave equation is derived by either eliminating the particle velocity \mathbf{v} or pressure p from Eq. (2.1) and (2.2). Eliminating the particle velocity result in,

$$\nabla \cdot \left[\frac{1}{\rho(\mathbf{r})} \nabla p(\mathbf{r}, t) \right] - \frac{1}{\kappa(\mathbf{r})} \frac{\delta^2 p(\mathbf{r}, t)}{\delta t^2} = s(\mathbf{r}, t), \quad (2.3)$$

with the source term,

$$s(\mathbf{r}, t) = \frac{\delta^2 q(\mathbf{r}, t)}{\delta t^2} - \nabla \cdot \left[\frac{\mathbf{f}(\mathbf{r}, t)}{\rho(\mathbf{r})} \right]. \quad (2.4)$$

Assuming a homogeneous and source free medium, Eq. (2.3) becomes,

$$\nabla^2 p(\mathbf{r}, t) - \frac{1}{c_p^2} \frac{\delta^2 p(\mathbf{r}, t)}{\delta t^2} = 0. \quad (2.5)$$

Here the acoustic wave velocity c_p [m s⁻¹] is defined as $\sqrt{\frac{\kappa}{\rho}}$.

Sometimes it is more convenient to view and manipulate the data in the frequency domain (Gisolf and Verschuur, 2016). This can be achieved by Fourier transforming Eq. (2.5),

$$\nabla^2 \hat{p}(\mathbf{r}, \omega) + \frac{\omega^2}{c_p^2} \hat{p}(\mathbf{r}, \omega) = 0, \quad (2.6)$$

which is called the Helmholtz equation. Here any variable in frequency domain is noted with a caret symbol, ω [Hz] is the angular frequency. See Appendix A for the definition of the Fourier transform. A typical solution to the Helmholtz equation are plane waves. These are governed by,

$$\hat{p}(\mathbf{r}, \omega) = \hat{W}(\omega) e^{-j\mathbf{k}\cdot\mathbf{r}}, \quad (2.7)$$

with,

$$\mathbf{k}\cdot\mathbf{r} = k_x r_x + k_y r_y + k_z r_z, \quad (2.8)$$

j being the imaginary unit, \mathbf{k} the wave vector, \mathbf{r} the Cartesian unity vector $[r_x, r_y, r_z]^T$, and \hat{W} the Fourier transform of the source signal, often called the source wavelet.

2.1.2. Elastic media

Waves in elastic media propagate according to the elastic wave equation. The derivation is significantly more complex compared to its acoustic counterpart. Because this does not introduce more insight for this thesis, the derivation is omitted and can be found in literature (Bath, 2013). The elastic wave equation in an isotropic, source free, slowly varying medium ($\nabla\lambda \approx 0$ and $\nabla\mu \approx 0$) equals to,

$$\rho(\mathbf{r}) \frac{\delta^2 \mathbf{u}(\mathbf{r}, t)}{\delta t^2} = (\lambda + 2\mu) \nabla(\nabla \cdot \mathbf{u}(\mathbf{r}, t)) - \mu \nabla \times \nabla \times \mathbf{u}(\mathbf{r}, t), \quad (2.9)$$

with λ [$\text{kg m}^{-1} \text{s}^{-2}$] and μ [$\text{kg m}^{-1} \text{s}^{-2}$] the Lamé constants,

$$\lambda = \frac{\sigma E}{(1 - 2\sigma)(1 + \sigma)}, \quad \mu = \frac{E}{2(1 + \sigma)}. \quad (2.10)$$

Here σ [-] and E [$\text{kg m}^{-1} \text{s}^{-2}$] are the Poisson's ratio (ratio between axial strain and transverse strain) and Young's modulus (relation between stress and strain), respectively (Bath, 2013). $\nabla \cdot \mathbf{u}$ describes the volumetric deformation whereas $\nabla \times \mathbf{u}$ characterizes the shearing deformation. Eq. (2.9) has two solutions, namely pressure waves (P) and shear waves (S). In P waves the particles displacement is parallel to the direction of wave propagation. For S waves this excitation is perpendicular to the direction of the wave. In homogeneous media these waves travel independent from each other according to their own wave equation. These equations can be derived by taking the curl for P waves or divergence for S waves of Eq. 2.9 (Bath, 2013). Applying the curl and using $\nabla \cdot (\nabla \times \mathbf{u}) = 0$ results in the P wave equation,

$$\nabla^2 (\nabla \cdot \mathbf{u}(\mathbf{r}, t)) - \frac{1}{c_p^2} \frac{\delta^2 (\nabla \cdot \mathbf{u}(\mathbf{r}, t))}{\delta t^2} = 0. \quad (2.11)$$

Applying the divergence and using $\nabla \times \nabla \times \mathbf{u} = \nabla \nabla \cdot \mathbf{u} - \nabla^2 \mathbf{u}$ gives rise to the S wave equation,

$$\nabla^2 (\nabla \times \mathbf{u}(\mathbf{r}, t)) - \frac{1}{c_s^2} \frac{\delta^2 (\nabla \times \mathbf{u}(\mathbf{r}, t))}{\delta t^2} = 0. \quad (2.12)$$

Here c_p [m s^{-1}] and c_s [m s^{-1}] are the acoustic and shear wave velocities respectively,

$$c_p = \sqrt{\frac{\lambda + 2\mu}{\rho}} < \sqrt{\frac{\mu}{\rho}} = c_s. \quad (2.13)$$

The total wave equation in elastic media can be written as a summation over P and S waves (Bath, 2013),

$$\frac{\delta^2 \mathbf{u}(\mathbf{r}, t)}{\delta t^2} = \underbrace{c_p^2 \nabla(\nabla \cdot \mathbf{u}(\mathbf{r}, t))}_{\text{P waves}} - \underbrace{c_s^2 \nabla \times (\nabla \times \mathbf{u}(\mathbf{r}, t))}_{\text{S waves}}. \quad (2.14)$$

2.1.3. Reflection and Transmission

Waves reflect and transmit upon a change in impedance. Reflection coefficient (R) and transmission coefficient (T) for both P and S waves at normal incidence become,

$$R = \frac{Z_{i+1} - Z_i}{Z_{i+1} + Z_i}, \quad T = \frac{2Z_{i+1}}{Z_{i+1} + Z_i}, \quad (2.15)$$

with Z [$\text{kg m}^{-2} \text{s}^{-1}$] the impedance ($Z_p = \rho c_p$ for P waves and $Z_s = \rho c_s$ for S waves). Here the subscript i denotes the media in which the wave reflects, $i + 1$ denotes the media to which (a part of) the wave transmits. It is important to note the possibility of a negative reflection coefficient, i.e. when $Z_{i+1} - Z_i < 0$.

Eq. (2.15) is only valid for waves intersecting a boundary parallel to the normal. The reflection and transmission coefficients of P waves under oblique incidence in acoustic media are,

$$R = \frac{Z_{i+1} \cos(\theta_i) - Z_i \cos(\theta_{i+1})}{Z_{i+1} \cos(\theta_i) + Z_i \cos(\theta_{i+1})}, \quad T = \frac{2Z_{i+1} \cos(\theta_i)}{Z_{i+1} \cos(\theta_i) + Z_i \cos(\theta_{i+1})}, \quad (2.16)$$

with θ_i [rad] and θ_{i+1} [rad] the angle of incidence and transmission respectively. See Appendix B for the derivation.

The elastic equivalent of angle-dependent reflection and transmission coefficient like Eq. (2.16) are not so straight forward. Here there is not only angle-dependency, but also exchange between P and S waves. These complex relations are described by the Zoeppritz equations (Aki and Richards, 2002). Due to the complexity and lack of insight these equations are omitted. Note that reflection and transmission of waves in acoustic media are also described by the Zoeppritz equations. However, these adhere to a special case where there is no propagation of shear waves, thus $c_s = 0$.

2.2. Standing wave theory

Plane waves will resonate between two reflective boundaries (R_1 and R_2) according to the standing wave theory. This concept already dates back to the 19th Century (Scott, 2006). The resonating waves carry information about the media parameters wave velocity and thickness. Because the resonating frequency is highly related to a phase shift at reflection, three cases need to be explored. Namely $R_1 \cdot R_2 > 0$ ($R_1 > 0$ & $R_2 > 0$ and $R_1 < 0$ & $R_2 < 0$), and $R_1 \cdot R_2 < 0$.

1. $R_1 > 0$ and $R_2 > 0$

When both of the reflection coefficients are positive, waves resonate according to,

$$f = n \frac{c}{2d}, \quad (2.17)$$

with f [Hz] the resonance frequency, c the wave velocity, d [m] the distance between the two reflective boundaries, and n a positive integer. $f(n = 1)$ describes the first harmonic (also called fundamental frequency), $f(n = 2)$ describes the second harmonic and so on. A visualization of the first three harmonics are shown in Fig. 2.1a-c.

2. $R_1 \cdot R_2 < 0$

When one of the reflection coefficients is negative, Eq. (2.17) is expanded to,

$$f = (2n - 1) \frac{c}{4d}. \quad (2.18)$$

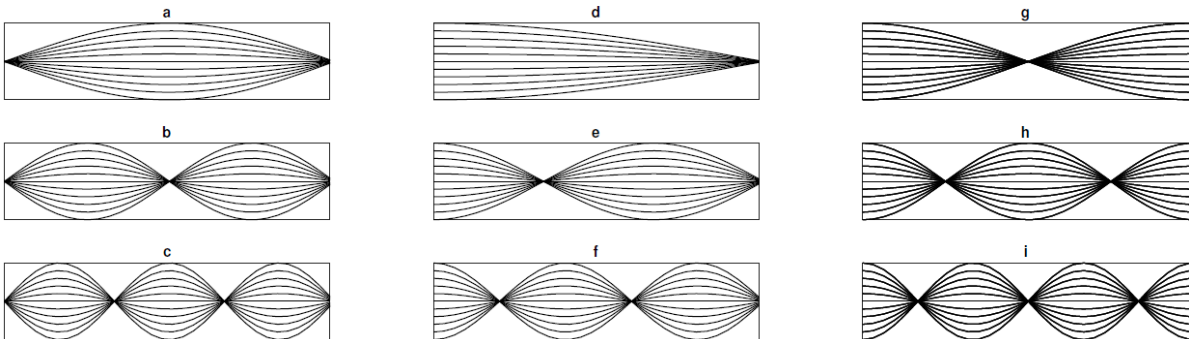


Figure 2.1: Resonance frequency visualized for the first three harmonics. Top $n = 1$, centre $n = 2$, bottom $n = 3$ taken for two positive reflection coefficients (left), one negative reflection coefficient on the left side of the domain (middle), and two negative reflection coefficients (right).

This equation is called the extended version of the standing wave theory. A wave reflecting with a negative reflection coefficient will experience a phase shift of $\pi/2$. The first three harmonics with a negative reflection on the left side of the domain are shown in Fig. 2.1d-f.

3. $R_1 < 0$ and $R_2 < 0$

Whenever both reflection coefficients are negative, a phase shift occurs at both sides of the domain. This will result in the same resonance frequency as in Eq. (2.17). The difference here is a total phase shift of π , as shown in Fig. 2.1g-i.

These relations are simple for a single, homogeneous layer. However, they become less intuitive whenever additional layers are added. As an example, a transmitted phase shifted wave can either (partly) cancel (destructive) or amplify (constructive) its encountering wave. This will happen for every wave at any given place and time. It is for this reason the standing wave theory is not very suitable for calculating the resonance peaks of multilayered systems. There are, however, simulation methods that can model wave propagation in any domain. These models can be used to get the desired frequency response and are explained in the next chapter.

2.3. Multichannel measurements

The proposed inversion scheme, which will be explained in Chapter 4, uses a forward model to simulate the wave propagation in a vertically layered medium. Simulating the response of a point source is a two dimensional problem (actually this is a three dimensional problem, however in this study only a two dimensional domain is considered). This is computationally very expensive. Plane wave responses can be simulated for one dimension and require almost no computation time. This will accelerate the inversion scheme considerably. However, implementing this forward model requires extra steps to interpret the received spherical wave data as plane wave responses. Here multichannel measurements are essential. This can be proven using Fourier theory. Recall the transformation of a signal d from receiver space-time domain to wavenumber-frequency domain,

$$\hat{D}(k_x, \omega) = \int_{-\infty}^{\infty} \int_{-\infty}^{\infty} d(x, t) e^{j(k_x x - \omega t)} dx dt. \quad (2.19)$$

By setting the wavenumber k_x to zero, Eq. (2.19) becomes,

$$\hat{D}(0, \omega) = \int_{-\infty}^{\infty} \int_{-\infty}^{\infty} d(x, t) e^{-j\omega t} dx dt = \int_{-\infty}^{\infty} \hat{D}(x, \omega) dx. \quad (2.20)$$

This is no more than summing over the entire measurement plane. However, measuring over an infinite plane is impossible and luckily unnecessary. Fig. 2.2 shows an example of a recorded wavefield of a finite domain. This wavefield is divided into three sections: S1, S2, and S3. S1 is called the 1th Fresnel zone. This is part of the wave which is recorded first. Due to the geometric spreading this is also the most horizontal part of the wavefield. Section S2 contains the wavefields at the boundaries of the domain. The remaining wavefield between S1 and S2 is denoted by S3. Eq. (2.20) can be rewritten as a summation over these sections,

$$\hat{D}(0, \omega) = \int_{S_{total}} \hat{D}(0, \omega) dx = \int_{S1} \hat{D}(x, \omega) dx + 2 \int_{S2} \hat{D}(x, \omega) dx + 2 \int_{S3} \hat{D}(x, \omega) dx. \quad (2.21)$$

The integral over S3 is zero. There is a balance between peaks and troughs; destructive addition. However, this is not applicable in S1 and S2. The peaks in the 1th Fresnel zone have no counteracting troughs. Integrating over S1 will therefore result in a non zero term. The same occurs in S2. However, in contrary to S1, this is a simulation artefact due to a limited computation domain. Here there is no balance between positive and negative amplitude. Fortunately, this can be suppressed by tapering the edges of the recorded wavefield. Studies to the 1th Fresnel zone date back decades (Sheriff, 1985; Lindsey, 1989; Sheriff, 1996). However, these all describe seismic applications only. Studies to the 1th Fresnel zone in these multilayered systems are non-existing. This zone should be found empirically until further research is available.

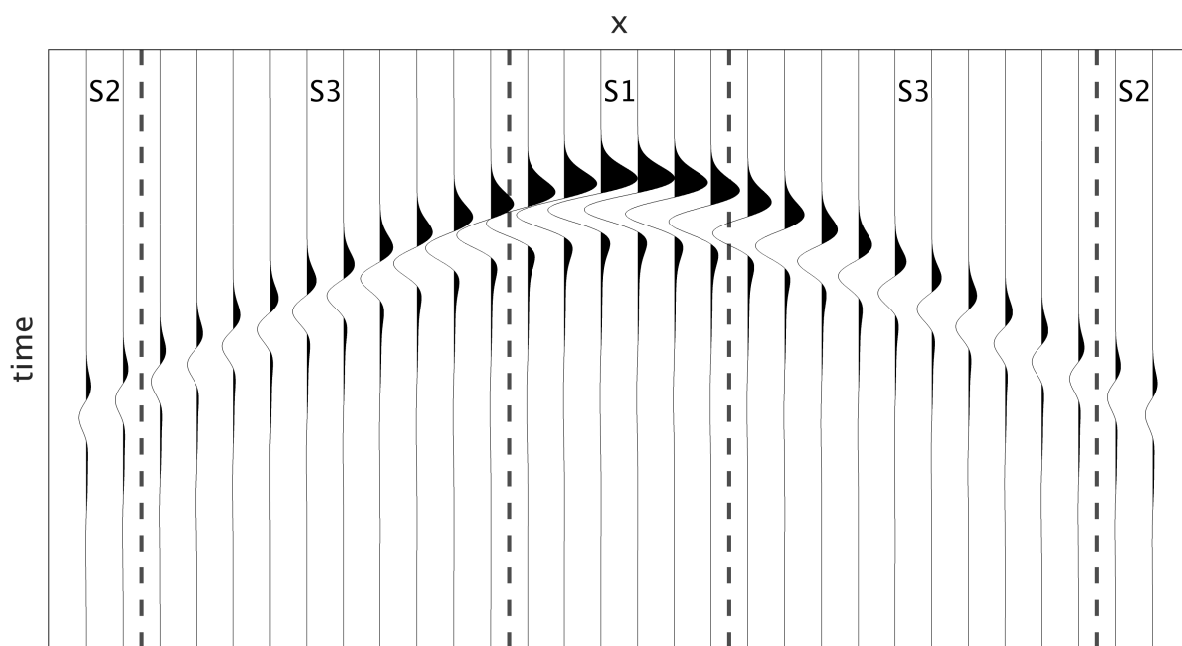


Figure 2.2: Example of a recorded wavefield of a domain with one reflective boundary. (S1) 1th Fresnel zone, (S2) wavefield at the boundary, (S3) the remaining wavefield.

3

Modelling

The previous chapter listed the limitation of the standing wave theory for multilayered systems. Therefore, other approaches need to be explored. This chapter provides two simulation methods which gain insight in the frequency response of a layered media. First, an Elastic Finite Difference (EFD) method is introduced. Next, the simplified full wavefield modelling scheme is explained.

3.1. Elastic Finite Difference model

Wave propagation can be modelled using a so-called finite difference method as proposed by Virieux (1986). Here the elastodynamic equations are transformed into a first-order hyperbolic system. The wave equation in acoustic media is defined through the first-order linearized systems of Hooke's and Newton's law,

$$\frac{\delta \dot{u}_x}{\delta t} = -\frac{1}{\rho} \frac{\delta P}{\delta x}, \quad (3.1a)$$

$$\frac{\delta \dot{u}_z}{\delta t} = -\frac{1}{\rho} \frac{\delta P}{\delta z}, \quad (3.1b)$$

$$\frac{\delta P}{\delta t} = -\frac{1}{\kappa} \left[\frac{\delta \dot{u}_x}{\delta x} + \frac{\delta \dot{u}_z}{\delta z} \right], \quad (3.1c)$$

with \dot{u}_x , \dot{u}_z the particles velocity in x and z-direction, respectively. The temporal derivative can be approximated using a 2nd order scheme,

$$\frac{\delta P}{\delta t} \approx \frac{P((I + \frac{1}{2})\Delta t) - P((I - \frac{1}{2})\Delta t)}{\Delta t}, \quad (3.2)$$

with I the time step and Δt the time step size. The spatial derivative can be approximated with the 4th order centralized Crank-Nicolson approximation. This requires a staggered grid shown in Fig. 3.1 for updating \dot{u}_x and \dot{u}_z , and Fig. 3.2 for updating P . The 4th order Crank-Nicolson approximation is a linear combination of four Taylor expansions around $x=0$ (Fornberg, 1988). These are,

$$P(x + \frac{\Delta x}{2}) \approx P(x) + \frac{\Delta x}{2} \frac{\delta P}{\delta x} + \frac{\Delta x^2}{2^2 \cdot 2!} \frac{\delta^2 P}{\delta x^2} + \frac{\Delta x^3}{2^3 \cdot 3!} \frac{\delta^3 P}{\delta x^3} + \frac{\Delta x^4}{2^4 \cdot 4!} \frac{\delta^4 P}{\delta x^4} + \mathcal{O}(\Delta x^5), \quad (3.3a)$$

$$P(x - \frac{\Delta x}{2}) \approx P(x) - \frac{\Delta x}{2} \frac{\delta P}{\delta x} + \frac{\Delta x^2}{2^2 \cdot 2!} \frac{\delta^2 P}{\delta x^2} - \frac{\Delta x^3}{2^3 \cdot 3!} \frac{\delta^3 P}{\delta x^3} + \frac{\Delta x^4}{2^4 \cdot 4!} \frac{\delta^4 P}{\delta x^4} + \mathcal{O}(\Delta x^5), \quad (3.3b)$$

$$P(x + \frac{3\Delta x}{2}) \approx P(x) + \frac{3\Delta x}{2} \frac{\delta P}{\delta x} + \frac{3^2 \Delta x^2}{2^2 \cdot 2!} \frac{\delta^2 P}{\delta x^2} + \frac{3^3 \Delta x^3}{2^3 \cdot 3!} \frac{\delta^3 P}{\delta x^3} + \frac{3^4 \Delta x^4}{2^4 \cdot 4!} \frac{\delta^4 P}{\delta x^4} + \mathcal{O}(\Delta x^5), \quad (3.3c)$$

$$P(x - \frac{3\Delta x}{2}) \approx P(x) - \frac{3\Delta x}{2} \frac{\delta P}{\delta x} + \frac{3^2 \Delta x^2}{2^2 \cdot 2!} \frac{\delta^2 P}{\delta x^2} - \frac{3^3 \Delta x^3}{2^3 \cdot 3!} \frac{\delta^3 P}{\delta x^3} + \frac{3^4 \Delta x^4}{2^4 \cdot 4!} \frac{\delta^4 P}{\delta x^4} + \mathcal{O}(\Delta x^5). \quad (3.3d)$$

Subtracting Eq. (3.3b) from (3.3a) and Eq. (3.3d) from (3.3c) eliminates all even power terms,

$$H_1 = P(x + \frac{\Delta x}{2}) - P(x - \frac{\Delta x}{2}) \approx \Delta x \frac{\delta P}{\delta x} + 2 \frac{\Delta x^3}{24} \frac{\delta^3 P}{\delta x^3} + \mathcal{O}(\Delta x^5), \quad (3.4a)$$

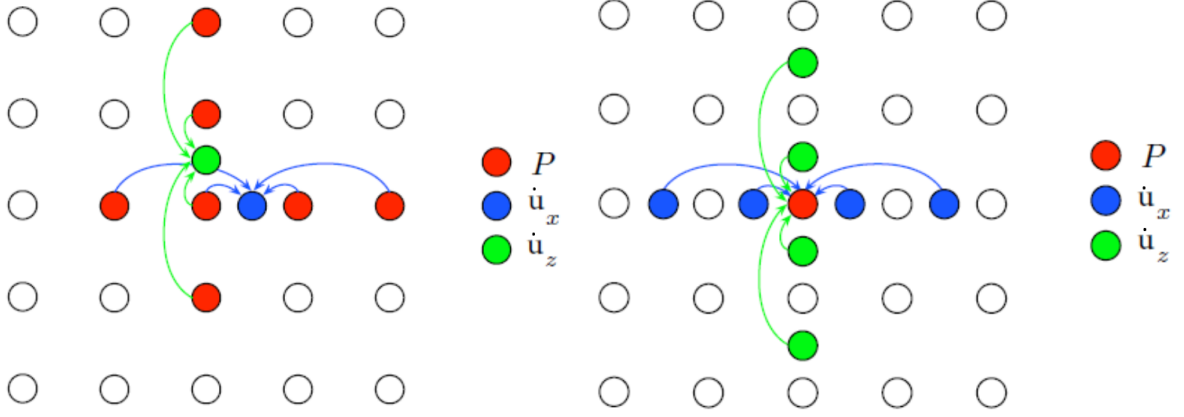


Figure 3.1: Staggered grid for updating the particles velocity \dot{u}_x and \dot{u}_z (Thorbecke and Draganov, 2011). Figure 3.2: Staggered grid for updating the pressure P (Thorbecke and Draganov, 2011).

$$H_2 = P\left(x + \frac{3\Delta x}{2}\right) - P\left(x - \frac{3\Delta x}{2}\right) \approx 3\Delta x \frac{\delta P}{\delta x} + 54 \frac{\Delta x^3}{24} \frac{\delta^3 P}{\delta x^3} + \mathcal{O}(\Delta x^5). \quad (3.4b)$$

The 4th order approximation can be derived by a linear combination of H_1 and H_2 . This eliminates all third order terms,

$$\frac{\delta P}{\delta x} + \mathcal{O}(\Delta x^5) \approx \frac{27H_1 - H_2}{24\Delta x} \approx \frac{27(P(x + \frac{\Delta x}{2}) - P(x - \frac{\Delta x}{2})) - P(x + \frac{3\Delta x}{2}) - P(x - \frac{3\Delta x}{2})}{24\Delta x} + \mathcal{O}(\Delta x^4). \quad (3.5)$$

With Eqs. (3.2) and (3.5) the particle velocity and pressure in Eq. (3.1)a-c can be calculated. Initially \dot{u}_x and \dot{u}_z are updated,

$$\dot{u}_x(t + \Delta t) = \dot{u}_x(t) + \Delta t \frac{\delta \dot{u}_x(t)}{\delta t} = \dot{u}_x(t) - \Delta t \frac{1}{\rho} \frac{\delta P}{\delta x}, \quad (3.6a)$$

$$\dot{u}_z(t + \Delta t) = \dot{u}_z(t) + \Delta t \frac{\delta \dot{u}_z(t)}{\delta t} = \dot{u}_z(t) - \Delta t \frac{1}{\rho} \frac{\delta P}{\delta z}. \quad (3.6b)$$

A source, if present, is added and the boundary conditions are implemented. Next the pressure P is updated according to Eq. (3.1)c and,

$$P\left(I + \frac{1}{2}\right)\Delta t = P\left(I - \frac{1}{2}\right)\Delta t + \Delta t \frac{\delta P}{\delta t}. \quad (3.7)$$

A source, if present, is added and \dot{u}_x and \dot{u}_z are updated again.

The Crank-Nicolson approximation is preferred over other methods because this is more robust, has high order of accuracy ($\mathcal{O}(\Delta x^4)$), and converges faster than the implicit and explicit finite different methods (Fadugba et al., 2013).

3.1.1. Convergence and stability criteria

For numerical time-marching schemes, which here means calculating \dot{u}_x , \dot{u}_z and P at time $T + \Delta t$ with information at time T , the convergence condition is given by the Courant number (Courant et al., 1967). This entails that a wave in one time step must not travel further than the distance between two grid points times the Courant number. For 4th order spatial derivatives as in Eq. (3.5) this number is 0.606 (Sei, 1995). This approximates to the following stability criteria,

$$\Delta t < \frac{0.606\Delta h}{c_{max}}, \quad (3.8)$$

with Δh the distance between two grid points in meter and c_{max} the maximum wave velocity.

Dispersion can be suppressed when the spatial discretization is five times smaller than the minimal wavelength (Alford et al., 1974),

$$\Delta h < \frac{\lambda_{min}}{5}. \quad (3.9)$$

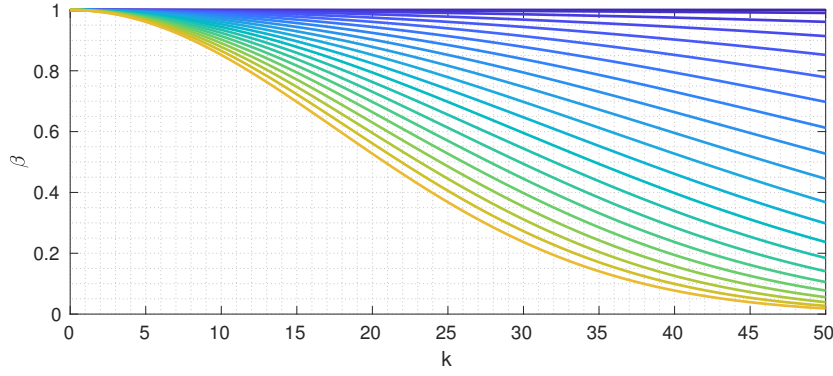


Figure 3.3: Suppression factor β for taper factor α between 0 (blue) and 2 (green) in increments of 0.1 over 50 grid points.

3.1.2. Boundary conditions

It is possible to choose the type of interaction between the modelled waves and the edges of the domain. This study makes use of absorbing boundaries. Here reflections from the sides of the model are avoided by suppressing the wave over k grid points. The degree of suppression, β , can be set with the taper factor α and equals,

$$\beta = e^{-\left(\alpha \cdot \frac{ik}{k_{max}}\right)^2}. \quad (3.10)$$

This is visualized in Fig. 3.3 for different taper factors over 50 grid points.

3.2. Wavefield Modelling via Bremmer Serie

Wave propagation can also be modelled by a Full Wavefield Modelling scheme (FWMod). FWMod is based on the Bremmer series which describes plane wave propagation of electromechanical waves in layered media (Bremmer, 1951). The concept is introduced for seismic applications and extended to angle dependency by Berkhout (2012). In this study a simplified FWMod (sFWMod) is introduced. Here only plane waves at normal incidence are assumed. The advantage of the sFWMod is the ability to use it as a forward model. This entails propagation between boundaries and not between gridpoints, reducing the computation time significantly.

At every boundary four wavefields are defined. These are the incoming wavefields \hat{P} and outgoing wavefields \hat{Q} . The reflection and transmission coefficients at each boundary are calculated according to Eq. (2.16). Propagation operators of wavefields between boundaries are denoted by \hat{W} , first introduced by Berkhout (1984). See Fig. 3.1 for a schematic overview of the operators and Table 3.2 for a description of the symbols. The incoming wavefields in boundary i are defined as,

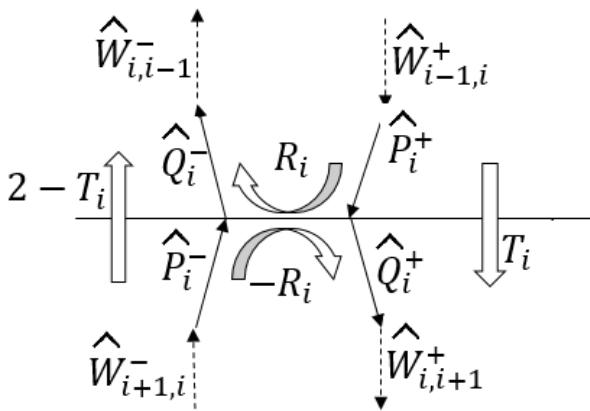


Table 3.1: Schematic view of the wavefields \hat{P} and \hat{Q} , reflection R and transmission T , and propagation operators \hat{W} .

Table 3.2: Symbols in the sFWMod scheme.

Symbol	Description
i	indices layer
\hat{P}_i^+	incoming wave field from above
\hat{P}_i^-	incoming wave field from below
\hat{Q}_i^+	down going wave field
\hat{Q}_i^-	up going wave field
\hat{R}_i	reflection coefficient
\hat{T}_i	transmission coefficient
$\hat{W}_{i-1,i}^+$	down going propagation operator
$\hat{W}_{i,i+1}^-$	up going propagation operator

$$\hat{P}_i^+(z, \omega) = \hat{W}_{i-1,i}^+(z, \omega) \hat{Q}_{i-1}^+(z, \omega), \quad (3.11a)$$

$$\hat{P}_i^-(z, \omega) = \hat{W}_{i+1,i}^+(z, \omega) \hat{Q}_{i+1}^+(z, \omega), \quad (3.11b)$$

with the propagation operators,

$$\hat{W}_{i-1,i}^+(z, \omega) = e^{-jk d_{i-1,i}}, \quad (3.12a)$$

$$\hat{W}_{i+1,i}^+(z, \omega) = e^{-jk d_{i,i+1}}. \quad (3.12b)$$

Here $d_{i-1,i}$ [m] is the distance between boundary $i-1$ and i . Note that $\hat{W}_{i-1,i}^+$ and $\hat{W}_{i,i-1}^-$ are identical. The outgoing wavefields are defined as,

$$\hat{Q}_i^+(z, \omega) = T_i \hat{P}_i^+(z, \omega) - R_i \hat{P}_i^-(z, \omega), \quad (3.13a)$$

$$\hat{Q}_i^-(z, \omega) = (2 - T_i) \hat{P}_i^-(z, \omega) + R_i \hat{P}_i^+(z, \omega), \quad (3.13b)$$

with T_i the downward facing transmission coefficient and R_i upward facing reflection coefficient. The downward facing reflection coefficient, R_i^\cap , is the negative value of its upward equivalent. The upward facing transmission coefficient equals,

$$T_i^\uparrow = 1 + R_i^\cap, \quad (3.14)$$

and can be written a function of the downward facing transmission coefficient, T_i ,

$$T_i^\uparrow = 1 + R_i^\cap = 1 - R_i^\cup = 1 - (T_i - 1) = 2 - T_i. \quad (3.15)$$

The relations in Eq. (3.11) and (3.13) can be written using the following matrix multiplication scheme;

$$\begin{bmatrix} \hat{P}_i^+ \\ \hat{P}_i^- \\ \hat{Q}_i^+ \\ \hat{Q}_i^- \end{bmatrix} = \begin{bmatrix} 0 & 0 & 0 & 0 & 0 & 0 & \hat{W}_{i-1,i}^+ & 0 & 0 & 0 & 0 & 0 \\ 0 & 0 & 0 & 0 & 0 & 0 & 0 & 0 & 0 & 0 & \hat{W}_{i+1,i}^- & 0 \\ 0 & 0 & T_i & -R_i & 0 & 0 & 0 & 0 & 0 & 0 & 0 & 0 \\ 0 & 0 & R_i & 2 - T_i & 0 & 0 & 0 & 0 & 0 & 0 & 0 & 0 \end{bmatrix} \begin{bmatrix} \hat{P}_{i-1}^+ \\ \hat{P}_{i-1}^- \\ \hat{P}_i^+ \\ \hat{P}_i^- \\ \hat{P}_{i+1}^+ \\ \hat{P}_{i+1}^- \\ \hat{Q}_{i-1}^+ \\ \hat{Q}_{i-1}^- \\ \hat{Q}_i^+ \\ \hat{Q}_i^- \\ \hat{Q}_{i+1}^+ \\ \hat{Q}_{i+1}^- \end{bmatrix} + \mathbf{S}. \quad (3.16)$$

Eq. (3.16) can be extended for any number of layers. Introducing a source wavelet is done by adding the vector \mathbf{S} to the right hand side. This vector contains one nonzero element at the position where the source wavelet is introduced to the medium. It should be noted that Eq. (3.16) is valid for one frequency only and should be repeated for every component in the source signal. Attenuation can be introduced by adding a negative imaginary value to the wave vector. However, in this study no attenuation is added. It is possible to substitute the matrix multiplication to an analytical function. This is called the Kennett model (Kennett, 1979). However, this model becomes very complex rather quickly and does not introduce more insight for this thesis. Therefore, a derivation is omitted. An example of the Kennett model of a five layer system can be seen in Appendix C.

4

Inversion

Full Waveform Inversion (FWI) is a very popular method for building velocity models. In FWI the difference between the received signal and modelled wavefronts is minimized. The amplitude and phase of the wavefront provide additional information to create a local differential approach for calculating the gradient and Hessian operators (Virieux and Operto, 2009). However, this method requires certain knowledge about the source. When this knowledge is absent, or when the source wavelet is not constant over multiple measurements, and no distinction between arrivals can be made (see Fig. 1.1), standard FWI fails. This study proposes two inversion schemes which use the peaks (and troughs) of the absolute frequency spectra of received IE data. Here the phase is omitted as it is strongly linked to the source signal. The first inversion scheme uses a function that links one frequency peak to domain parameters. The second scheme uses the peaks and troughs of the entire received frequency spectrum. Here additional pre-processing steps are proposed and an iterative solver to update the velocity model is introduced.

4.1. Inversion Scheme 1: Single peak inversion

The resonance frequency of each layer can be calculated using the (extended version of the) standing wave theory as introduced in Chapter 2. This hints that every multilayered system also has its own overall resonating frequency. This frequency can be determined using the proposed modelling schemes given in Chapter 3. A function can be created which characterizes a peak position to certain domain parameters. An advantage to this method is the possibility to create this function offline using an accurate EFD scheme. Inversion can be done instantly with the created function or within a few iteration steps once the shape of the function can be estimated. A peak can be chosen above a certain threshold. However, this condition is strongly related to the source wavelet. It is more robust to select the highest peak within a specific frequency window.

4.2. Inversion Scheme 2: Minimizing an objective function

Single peak inversion has its disadvantage that one peak might not be unique to a single set of parameters. Furthermore, all additional information in terms of frequency peaks and troughs is discarded. This information might be useful to increase the accuracy or is even essential to create a sufficient objective function. The obvious next step is to create an inversion scheme that considers all peaks and troughs of the frequency spectra. This approach is explored in the second inversion scheme. A block diagram minimizing the objective function is shown in Figure 4.1. If a point source is used, edges are tapered and all receivers are summed in order to mimic a plane wave response (see Chapter 2). When a plane wave is induced, only one reflection signal (trace) is selected. The error between the measured signal and forward model response is defined as,

$$J = \sum_{\omega} \|f(\hat{P}_{measured}(\omega)) - f(\hat{P}_{modelled}(\omega))\|^2, \quad (4.1)$$

with f a suitable set of pre-processing steps. $\hat{P}_{measured}$ is the measured frequency spectra (either an average over all receivers or a single trace, depending on the source). $\hat{P}_{modelled}$ is the frequency spectra of the plane wave response created with the forward model. The pre-processing steps are necessary to remove the impact of the source wavelet. These also enhances the peaks and troughs position. In this study the following

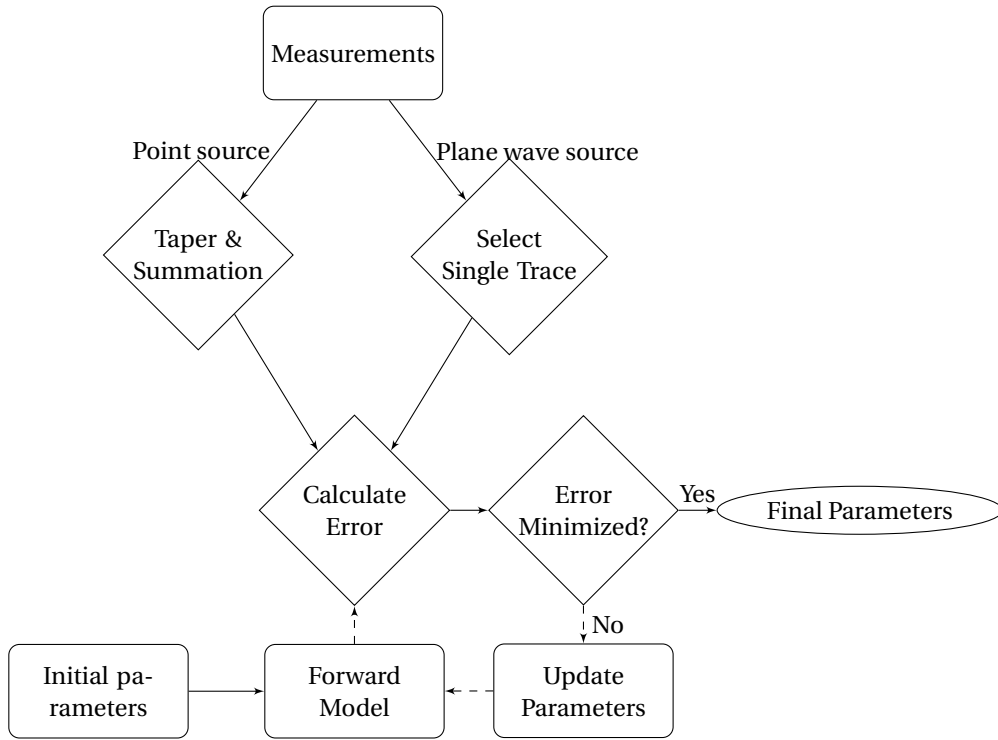


Figure 4.1: Block diagram for minimizing the objective function.

steps are chosen. Initially the moving mean is subtracted from the absolute spectrum. This leaves the peaks and troughs only, which we call $\Delta(\omega)$, being the normalized difference between absolute spectrum and its moving mean. These are enhanced and small amplitude differences are suppressed using the normalized compression function,

$$C(\Delta) = \frac{\text{atan}(\gamma \Delta)}{\max(\text{atan}(\gamma \Delta))}, \quad (4.2)$$

where γ is a scaling factor controlling the saturation. The compression function for different scaling factors is visualized in Fig. 4.2. An example of the applied pre-processing steps is shown in Fig. 4.3.

Minimizing the objective function is done by a steepest descent method, see Algorithm 1. The parameters for which the algorithm finds a minimum are the domain parameters, i.e. acoustic wave velocity and thickness of each layer, stored in the vector \mathbf{m} . The total gradient is calculated by a weighted average of all individual

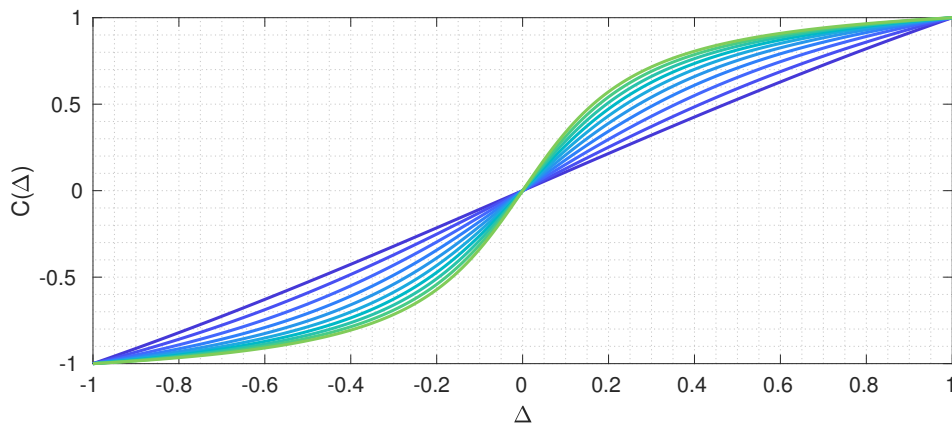


Figure 4.2: Compression function for different scaling factors γ between 0 (blue) and 5 (green) in increments of 0.5. Δ is the normalized difference between the absolute spectrum and its moving mean.

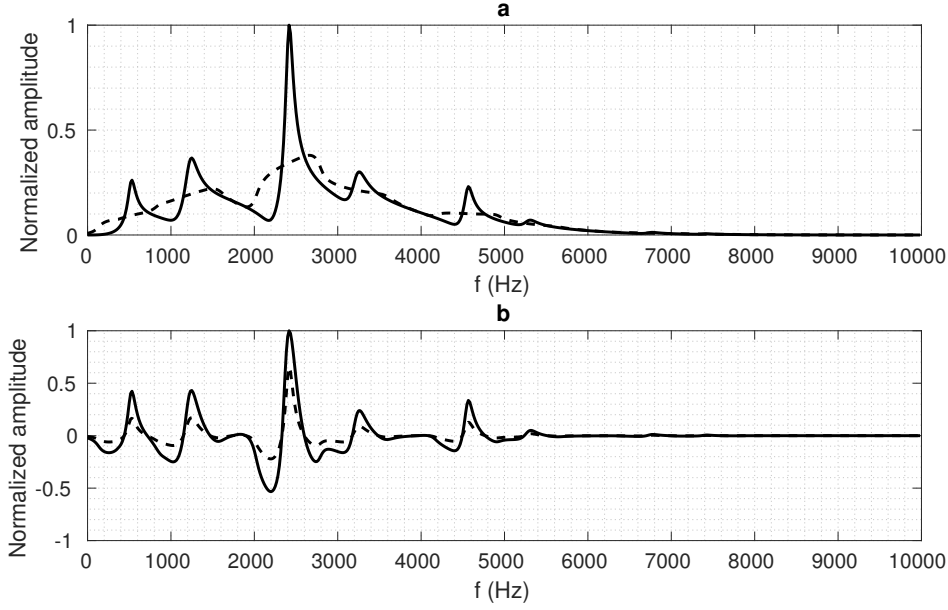


Figure 4.3: Example of a frequency spectra with and without pre-processing steps. (a) the absolute spectrum (solid) and the moving mean (dashed). (b) normalized difference between the absolute spectrum and its moving mean, Δ , without (dashed) and with compression function (solid). Here the moving mean is created with a window size of 750 Hz, γ equals 3.

gradients. These are calculated by a finite difference scheme, see Algorithm 2. Whenever a zig-zag pattern occurs, i.e. if two elements of consecutive gradient have opposite sign, the step size in that iteration is halved. Multiple start positions are used to decrease the possibility of ending in a local minima.

The plane wave response of a multilayered system does not adhere to the (extended version of the) standing wave theory. However, in layers with small travel times high frequency standing waves are present. These do affect the measured signal according to Eq. (3.16). The level of sensitivity for individual layers can be tested with a sensitivity analysis. Here the variables of each layer are changed individually. A change in frequency response is a measure of sensitivity. This is a quick way to determine the required source bandwidth and usability of the IE method for imaging specific layers.

Algorithm 1: Steepest descent

Result: Domain parameters

Input: Set starting parameters $\{\mathbf{m}_0^1, \dots, \mathbf{m}_0^N\}$,
step size β

for N starting positions **do**

 Calculate gradient: \mathbf{g}_i ;

while No minimum reached **do**

 Update parameters: $\mathbf{m}_{i+1} = \mathbf{m}_i + \beta \mathbf{g}_i$;

 Calculate gradient: \mathbf{g}_{i+1} ;

foreach element k of \mathbf{g}_{i+1} **do**

if $g_i^k \cdot g_{i+1}^k < 1$ **then**

$m_{i+1}^k = m_i^k + \frac{\beta}{2} \cdot g_{i+1}^k$;

 Calculate new gradient: g_{i+1}^k ;

else

$m_{i+1}^k = m_{i+1}^k$

 Pick M parameters with lowest error

Algorithm 2: Calculating gradient

Result: \mathbf{g}_{i+1}

Input: \mathbf{m}_{i+1} , step size δ

foreach element k of \mathbf{m}_{i+1} **do**

${}^1 h_{i+1}^k = m_{i+1}^k$;

 Forward Model(${}^1 h_{i+1}^k$);

 Calculate Error = ${}^1 e_{i+1}^k$;

${}^2 h_{i+1}^k = m_{i+1}^k + \delta m_{i+1}^k$;

 Forward Model(${}^2 h_{i+1}^k$);

 Calculate Error = ${}^2 e_{i+1}^k$;

$g_{i+1}^k = \frac{{}^2 e_{i+1}^k - {}^1 e_{i+1}^k}{\delta}$

5

Results

The proposed inversion methods are tested on synthetic data of a multilayered furnace wall. It is impossible to do control measurements on an operational furnace. Therefore the EFD model `fde1modc` (Thorbecke and Draganov, 2011) is used to create synthetic data. It is worth noting that this model solves the 2-D Greens function in a 3-D framework, measuring along a perpendicular plane. This results in an amplitude shift proportional to $k^{-1/2}$ due to different geometrical spreading (Berkhout, 1987). Properties of the individual layers as wave velocity and design thickness of every layer are shown in Table 5.1.

A Ricker wavelet with a peak frequency of 3 kHz and a maximum frequency of 10 kHz is introduced as source. Fig. 5.1 shows the normalized source wavelet in both time and frequency domain. The wavelet is created with the program `makewave`, which is provided in the package of `fde1modc` (Thorbecke, 1993). The input parameters are: $dt=1e-4$ ms, $nt=7000$, $w=g2$, and $fp=3$ kHz. The source is introduced at the air/refractory interface. A plane wave source is simulated using `fde1modc`'s plane wave option with sources spanning the entire width of the domain. Spherical waves are created by an array of 15 sources spanning 30 mm.

Receivers at the air/refractory interface record either pressure for acoustic modelling or particle velocity for elastic schemes. A sample frequency of 20 kHz is used to uphold the Niquist criteria (Cramér and Grenander, 1959). Due to the high computation times of the EFD model, only 10 ms of recording time is simulated. The frequency spectra are created using Matlab and its Fast Fourier Transform (MATLAB, 2018), and the resolution is increased to 9 Hz by adding zeros to the time signal.

First, the results of the sensitivity analysis is introduced. Next, the response of a plane wave source in `fde1modc` and `sFWMod` is compared and the two inversion methods are tested. Lastly, multichannel measurements with point sources are performed and compared to the plane wave response of `sFWMod`.

Table 5.1: Properties of the different layers in the refractory and liquid steel. Here the subscript p and s denote the acoustic and elastic properties, respectively. ¹Thicknesses according to design. ²Wave velocities are set to be constant, while in fact these are not due to a temperature gradient. The reflection and transmission coefficients are valid for plane waves at normal incidence only and are defined as in Fig. 3.1.

Layer	Thickness (mm) ¹	Density (kg/m ³)	Wave velocity (m/s) ²		Reflection		Transmission	
			c_p	c_s	R_p	R_s	T_p	T_s
Air	500	1.2	356	0	1	1	2	2
Steel shell	60	7800	5800	3250	-0.9	-0.9	0.1	0.1
Mortar joint	2	1200	1500	840	0.3	0.3	1.3	1.3
Graphite	350	1750	1900	1064	-0.15	-0.15	0.85	0.85
Ramming	40	1500	1650	924	0.5	0.5	1.5	1.5
Semi-graphite	750	2500	3000	1680	0.7	-1	1.7	0
Liquid steel	-	7700	5000	0				

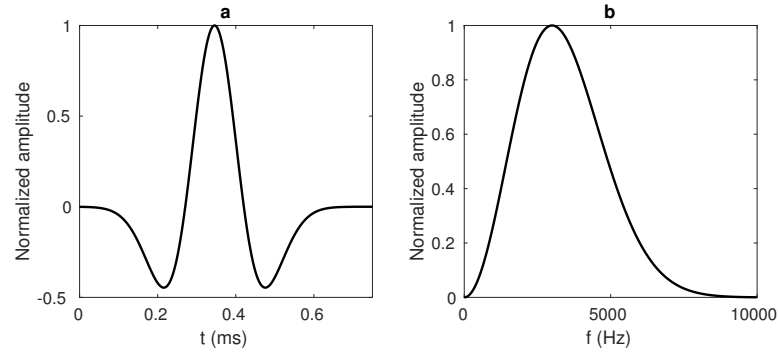


Figure 5.1: Source wavelet used in the experiment: Ricker wavelet with $dt=1e-4$ ms, $nt=7000$, a peak frequency of 3 kHz and a maximum frequency of 10 kHz in (a) the time domain and (b) as absolute frequency spectra.

5.1. Sensitivity analysis

The sensitivity analysis is performed by varying the individual parameters of each layer, i.e. density, wave velocity and thickness, between 70 and 130 percent of the design specifications (Table 5.1). Simulations are done with sFWMod due to the large number of calculated spectra. Only the acoustic case is studied, as only an acoustic source is considered. Even though this method is less accurate and valid for plane waves in acoustic domains only, it does provide fundamental information about the usability of the IE method. A single frequency spectra of a medium with the design specification is shown in Fig. 4.3a. Because this section tests the sensitivity of the IE method, no pre-processing steps are performed.

5.1.1. Density

The absolute spectra for varying densities are shown in Fig. 5.2. Fig 5.2a shows the spectra for varying density of the steel shell, Fig 5.2b of the mortar joint, etc. (see Fig. 1.2 for the schematic overview of the refractory). The spectra show IE is rather insensitive to a change of density. The lack of sensitivity can be explained as only the reflection and transmission coefficients depend on the density. Changing these coefficients will only affect relative amplitudes. Because the spectra is build up out of many reflected waves, these small amplitude differences make small changes in the spectra. However, when the densities are shifted to such an extend where the reflection or transmission experience a sign flip, bigger differences occur. This dependency is buried deep in Eq. (3.16). Simulations can provide information about the effect of a sign flip.

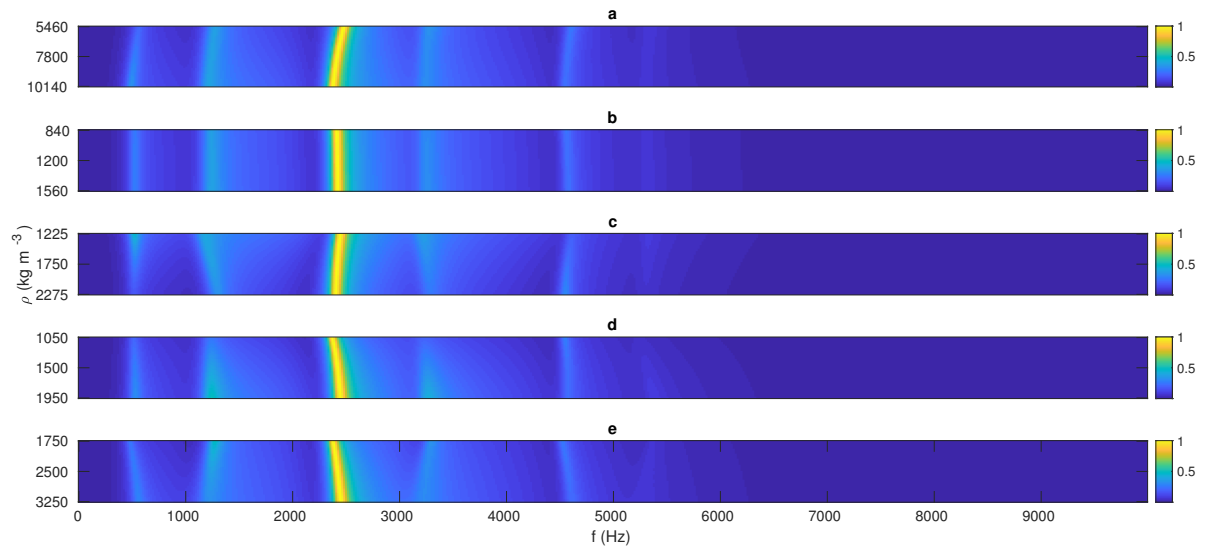


Figure 5.2: Absolute frequency spectra for varying densities between 70 and 130 percent of the design specification. (a) steel shell, (b) mortar joint, (c) graphite, (d) ramming layer, and (e) semi-graphite. All spectra are made with sFWMod.

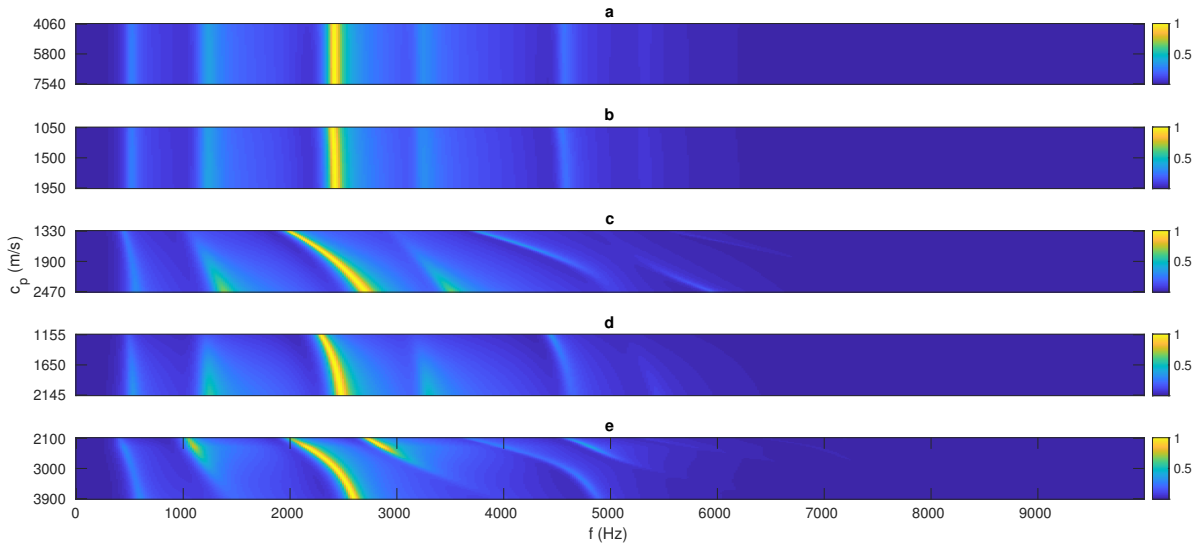


Figure 5.3: Absolute frequency spectra for varying wave velocities between 70 and 130 percent of the design specification. (a) steel shell, (b) mortar joint, (c) graphite, (d) ramming layer, and (e) semi-graphite. All spectra are made with sFWMod.

5.1.2. Wave velocity

Fig. 5.3 shows the spectra for varying wave velocities in the same layers as previous test. This shows the IE method is insensitive to a change in wave velocity in both the steel shell and mortar joint. These layers have very small travel times $\tau = d/c$, i.e. high frequency standing waves, which expresses itself in the propagation operator \hat{W} equal to one. For larger travel times, like in the graphite and semi-graphite layer, the phase of \hat{W} is non-zero. Small changes affect these propagation operators significantly. One could argue that a changing velocity also affects the reflection and transmission coefficients. This is true, however as shown before, these coefficients do not influence the frequency spectra significantly.

5.1.3. Thickness

The frequency spectra for varying thickness are shown in Fig. 5.4. The overall trend is similar as for changing velocities. However, the peaks are shifted in the opposite direction. The reason for this is simple; an increasing thickness d or decreasing wave speed c both result in a higher travel time τ . Consequently, both scenarios produce the same propagation operator which result in similar spectra. This introduces an important limitation; it is only possible to measure the ratio between thickness and wave velocity of the individual layers. Furthermore, the most sensitive layers have a standing wave frequency also present in the source wavelet. This is shown with the frequency of the graphite and semi-graphite layer. These have a fundamental frequency of approximately 5 and 3 kHz, respectively, while the fundamental frequency of the steel shell equals 130 kHz. It must be noted that the IE method does become more sensitive to layers whenever the fundamental frequency approximates the frequencies that are present in the source wavelet, e.g. the fundamental frequency of the ramming layer equals 23 kHz.

5.2. Inversion

The IE method is most sensitive to the graphite and semi-graphite thickness assuming fixed velocities. One could argue that the thickness of the ramming layer should also be taken into account as a trend is visible. Inverting for these thicknesses only is explored for reasons explained above. This reduces the overall number of variables from 15 to 3. First single peak inversion method is introduced with one variable only. Next an objective function is minimized. Initially the importance of the pre-processing steps are shown and the error surfaces for different graphite and semi-graphite layers is provided. Thereafter, this method is used to invert for the graphite, ramming, and semi-graphite thickness.

5.2.1. Single peak inversion

Fig. 5.5a shows the frequency spectra for varying semi-graphite thicknesses created with sFWMod (increased thickness domain compared to Fig. 5.4e). A function of peak position and thickness is created for the peaks

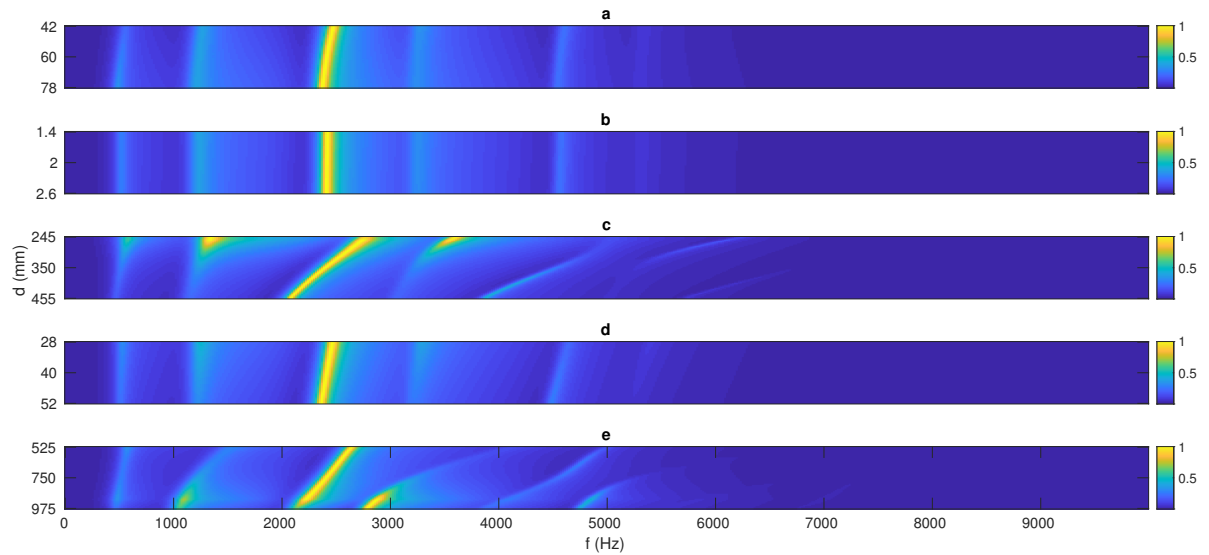


Figure 5.4: Absolute frequency spectra for varying thicknesses between 70 and 130 percent of the design specification. (a) steel shell, (b) mortar joint, (c) graphite, (d) ramming layer, and (e) semi-graphite. All spectra are made with sFWMod.

inside the rectangle box. The fitted function is shown in Fig. 5.5b. These figures already show a limitation of this method. One peak position is not unique to a single semi-graphite thickness. A peak at 2500 Hz corresponds to both 660 and 100 mm. However, a more restrictive limitation is the possibility to shift a single peak by varying different parameters (see the sensitivity analysis). It is for these reasons an inversion method based on one frequency peak is insufficient.

5.2.2. Minimizing an objective function

The second inversion method is tested on synthetic data created with `fde1modc`. Here plane waves are induced. sFWMod is used as forward model to make sure no inverse crime is committed (Wirgin, 2004). The importance of the pre-processing steps is introduced and the performance of the steepest descent method is tested.

Preprocessing steps

Figure 5.6a shows a received frequency spectra of `fde1modc` and sFWMod for similar parameters. The origin of the absence of the first peaks and the high resonating artefact in the `fde1modc` data are unknown. However, creating an inversion scheme regardless makes it more robust. Small differences in amplitude are suppressed

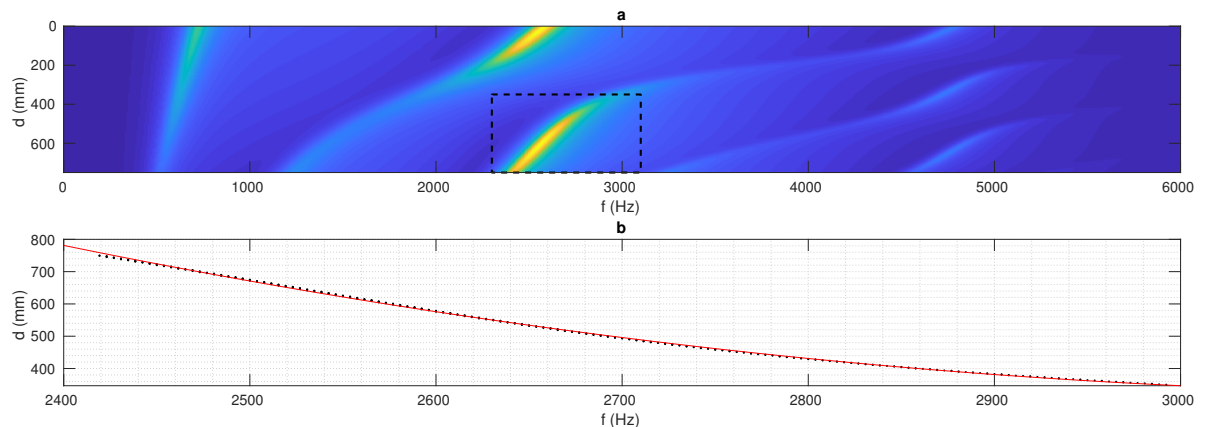


Figure 5.5: (a) absolute frequency spectra for varying semi-graphite thickness between 0 and 750 mm (made with sFWMod). The rectangle box indicates the region of interest for creating the function. (b) peak position versus semi-graphite thickness with the straight line being the fit.

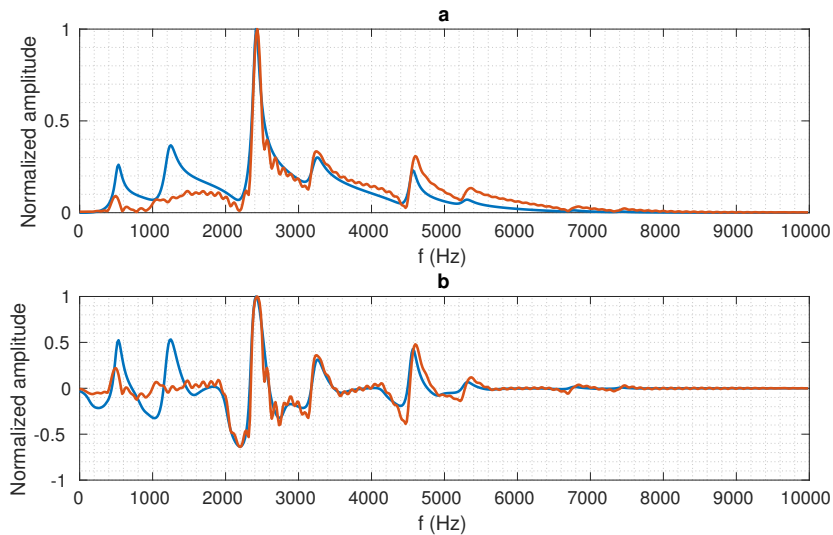


Figure 5.6: Example received frequency spectra for $f_{delmodc}$ (red) and $sFWMod$ (blue) with (a) no pre-processing steps, and (b) with pre-processing steps (frequency window of 750 Hz, γ equals 3).

with the suppression function. This is shown in Fig 5.6b.

The error between $f_{delmodc}$ and $sFWMod$ is calculated according to Eq. (4.1). Fig. 5.7a-b show the error surfaces without and with pre-processing steps for varying graphite and semi-graphite thicknesses. It is expected that the global minimum is situated in the centre of the image, as these are the input parameters of $f_{delmodc}$. However, Fig. 5.7a shows a minimum at the wrong place. This is not the case in Fig. 5.7b, which demonstrates the importance of the proposed pre-processing steps. The valley shape global minimum can be explained using the spectra in the sensitivity analysis. An upwards frequency shift by decreasing the thickness of one layer can be (partly) cancelled by increasing another.

The overall shape of the objective function will always have this valley-like structure. However, selecting different frequency window sizes for calculating the moving mean will change its width. This is shown in Fig. 5.8. High-order aberrations will be filtered out when a small window size is used. However, using a small window size means the moving mean will follow the signal more, and peaks and troughs will become less apparent after subtraction. Local minima are more easily created if these amplitudes are small. Expanding

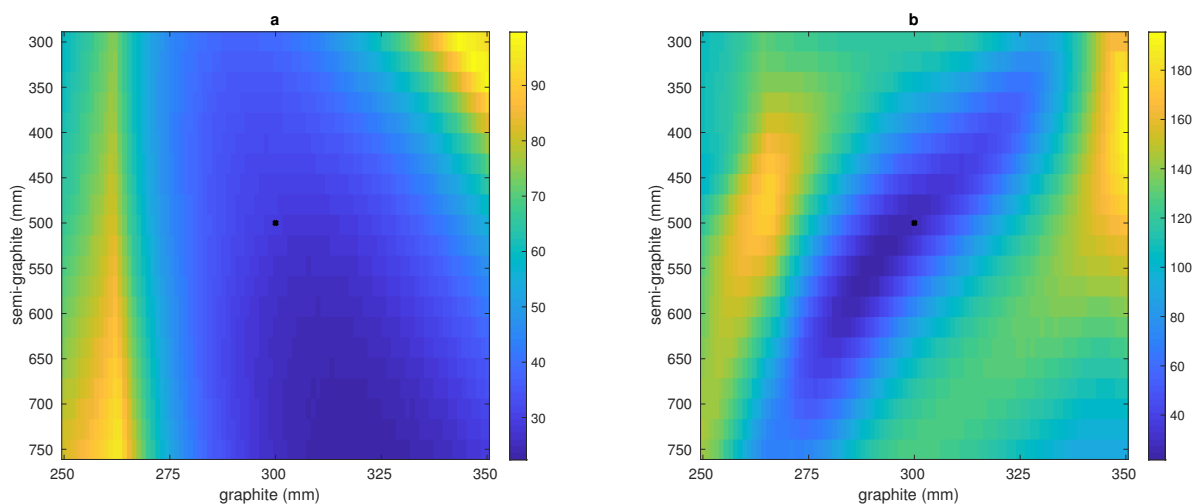


Figure 5.7: Error surfaces for varying graphite and semi-graphite thicknesses The dot represents the input parameters in $f_{delmodc}$. (a) no pre-processing, (b) applied pre-processing (window size of 700 Hz, γ equals 3).

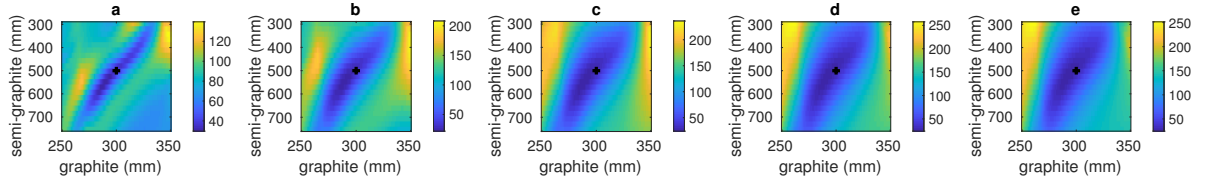


Figure 5.8: Error surfaces using various window sizes from (a) 300 Hz to (e) 2300 Hz in steps of 500 Hz.

the window size will not filter out the high-order aberrations but maintains the relative peak amplitudes. This results in fewer local minima on the cost of a larger, more flattened, global minimum.

Performance

The inversion method is tested on inverting for the thickness of the graphite, ramming, and semi-graphite layer. The parameters in `fdelmodc` are 300, 40, and 500 mm for the graphite, ramming layer, and semi-graphite layer, respectively. All other parameters are set as in Table 5.1. A plane wave is induced, and only the acoustic domain is considered. Due to the expected amount of local minima, 200 starting parameter sets $\{\mathbf{m}\}$ are chosen (see Algorithm 1). These are uniform randomly selected within a pre-defined domain ($200 \text{ mm} < \text{graphite} < 400 \text{ mm}$, $30 \text{ mm} < \text{ramming} < 50 \text{ mm}$, and $250 \text{ mm} < \text{semi-graphite} < 750 \text{ mm}$). Whenever the algorithm tries to find a minimum outside this domain, the iteration is aborted and a new parameter set is initialized.

The convergence plots for different frequency windows are shown in Fig. D.1. Only the 20 parameter sets with lowest error are selected. Data is visualized in Fig. D.2 and D.3 for all data and the best 20 sets, respectively. Statistics of the best 20 sets is presented in Table 5.2. Results are in line with the expected global minimum. Its position does not change upon choosing different frequency window sizes. The standard deviation of thickness of the ramming layer is significant compared to its mean value. This occurs because the IE method is rather insensitive to the thickness of this layer. Results for increasing scaling factors γ are shown in Figs. D.4, D.5, D.6 and Table 5.3. The method seems to become more accurate if a bigger scaling factor is chosen. However, due to the relative large standard deviation a real conclusion cannot be taken.

5.3. Multichannel measurements

Prior simulations were done with single channel measurements of a plane waves source at normal incidence in an acoustic domain. This section contains the comparison between the plane wave response and spherical wave response in both acoustic and elastic media. The spectra are created with `fdelmodc` with the parameters similar to the input values in the inversion scheme (300, 40, and 500 mm for the graphite, ramming layer, and semi-graphite layer, respectively). Reflections of the edges of the domain are suppressed by absorbing boundaries of 1500 grid points with a taper factor of 0.3. The time and frequency signal of acoustic media are shown in Fig. 5.9. Plane wave and spherical wave responses in elastic media are shown in Fig. 5.10. There is almost no difference between the acoustic and elastic plane wave spectra. This is expected as an acoustic plane wave is induced. At normal incidence there is no exchange between S and P waves (see Chapter 2). However, the spectra differ considerably when a point source is used. This shows that the angle dependent

Table 5.2: Statistics of the best 20 parameter sets with lowest error for different frequency window sizes. d_3 , d_4 , and d_5 represent the thickness of the graphite, ramming layer, and semi-graphite layer, respectively. A compression function with a scaling factor γ of 3 is used.

Window (Hz)	Error		d_3 (mm)		d_4 (mm)		d_5 (mm)	
	Mean	Std.	Mean	Std.	Mean	Std.	Mean	Std.
750	26	5	297	17	42	7	508	37
1000	27	5	297	17	42	6	507	37
1250	28	4	294	16	43	6	506	35
1500	28	4	294	16	42	6	509	34
1750	27	3	298	17	40	6	509	35
2000	27	3	296	17	40	6	517	33

Table 5.3: Statistics of the best 20 parameter sets with lowest error for different scaling factors γ in the compression function. d_3 , d_4 , and d_5 represent the thickness of the graphite, ramming layer, and semi-graphite layer, respectively. A frequency window size of 1000 Hz is used.

Scaling factor	Error		d_3 (mm)		d_4 (mm)		d_5 (mm)	
	Mean	Std.	Mean	Std.	Mean	Std.	Mean	Std.
1	12	2	295	16	41	6	519	42
2	19	3	294	17	42	6	514	38
3	27	5	297	17	42	6	507	37
4	36	7	299	18	42	7	495	28
5	46	10	302	20	41	7	498	36
6	55	11	302	20	40	7	499	36

reflection and transmission coefficients affect the spectra significantly.

Chapter 2 showed the theory of transforming a spherical wave response to its plane wave equivalent. This is done by tapering the edges and summing over the receiver plane. The edges of the aperture are tapered using a Tukey window with a cosine fraction of 0.6. Fig. 5.11a (acoustic) and 5.12a (elastic) show the averaged spectra over the entire width of the receiver plane without any tapering. Fig. 5.11b-d and 5.12b-d have increasing aperture widths (500, 1000, and 1500 mm) and do contain the above described taper. These figures clearly show the importance of tapering the signal at the edge of the receiver plane.

The spectra with different aperture widths in both the acoustic and elastic domain are also used as input of the inversion scheme. Results are shown in Table 5.4. It is already possible to successfully invert for acoustic data with an aperture width of 500 mm. The accuracy will increase when using a larger aperture. However, this trend is not visible in the elastic domain. One reason can be the presence of reflections from the sides of the computation domain which are not sufficiently absorbed and produce interference.

Table 5.4: Statistics of the best 20 parameter sets with lowest error for different aperture widths for a point source in the acoustic domain. d_3 , d_4 , and d_5 represent the thickness of the graphite, ramming layer, and semi-graphite layer, respectively. A frequency window size of 1000 Hz and a scaling factor of 3 is used.

Width (mm)	Error		d_3 (mm)		d_4 (mm)		d_5 (mm)	
	Mean	Std.	Mean	Std.	Mean	Std.	Mean	Std.
Acoustic								
500	55	8	299	20	39	8	470	42
1000	37	6	295	18	42	7	478	40
1500	29	7	298	19	42	7	480	40
Elastic								
500	64	5	304	21	43	7	485	43
1000	36	5	307	18	40	6	494	43
1500	34	6	310	22	42	7	459	41

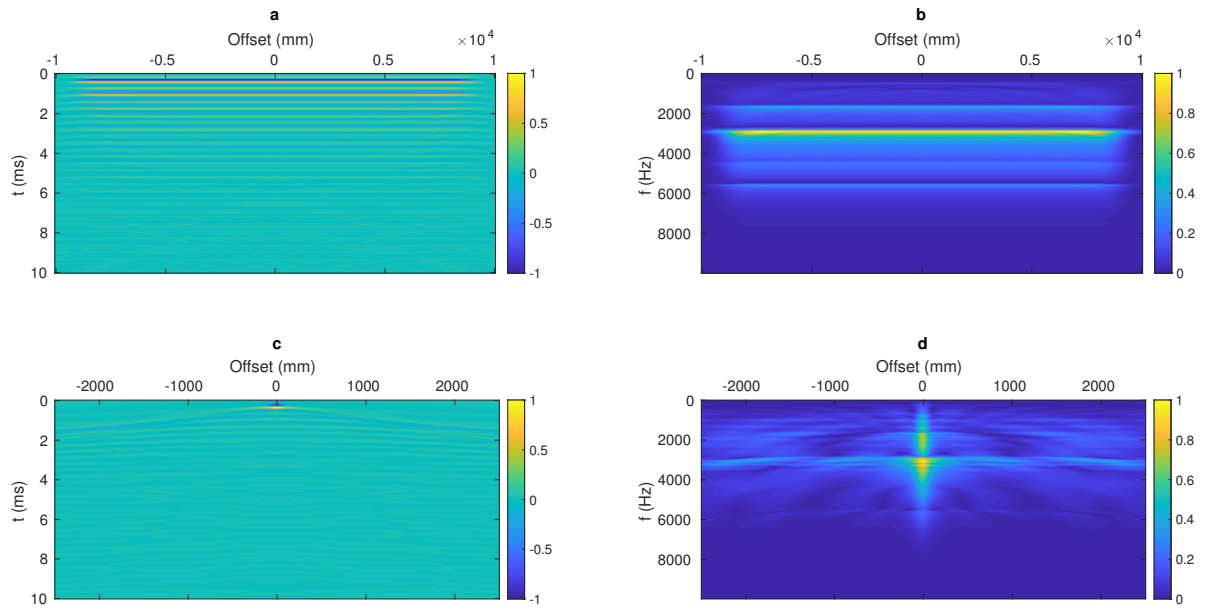


Figure 5.9: Received signal of multichannel measurements in the acoustic domain. Plane wave source in (a) the time domain and (b) the frequency domain. Point source in (a) the time domain and (b) the frequency domain.

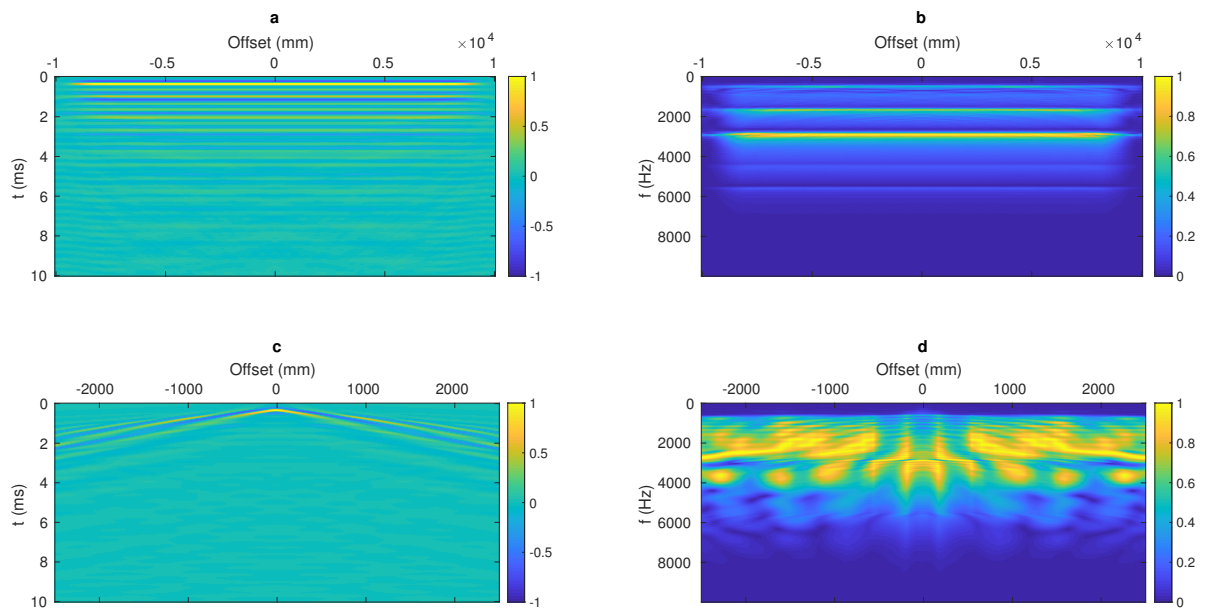


Figure 5.10: Received signal of multichannel measurements in the elastic domain. Plane wave source in (a) the time domain and (b) the frequency domain. Point source in (a) the time domain and (b) the frequency domain.

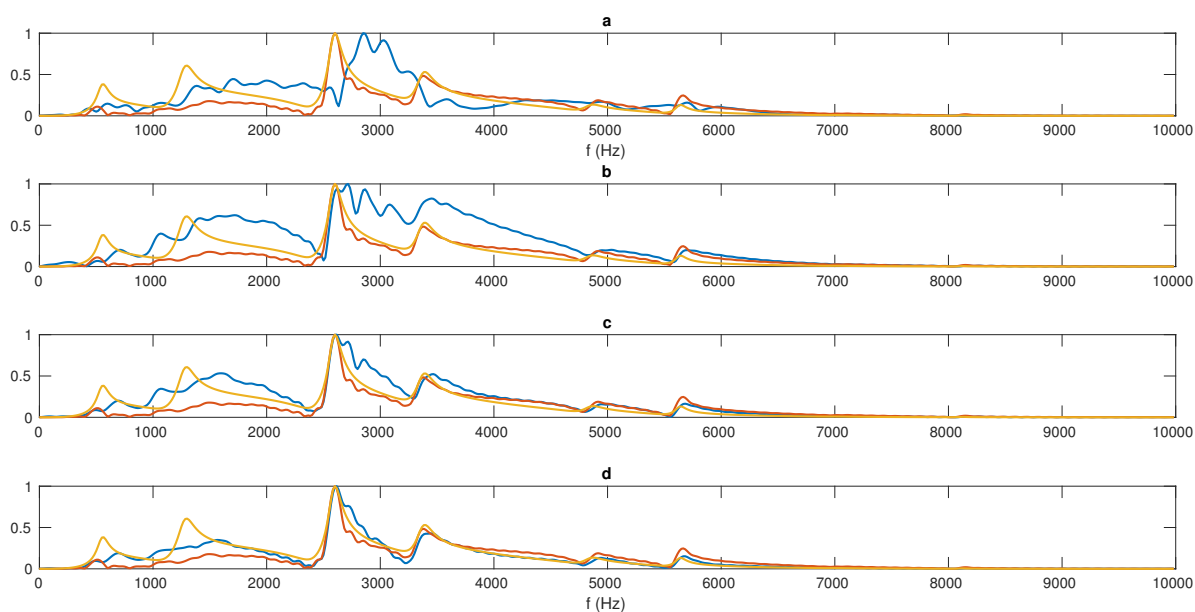


Figure 5.11: Normalized frequency responses for the acoustic domain. sFWMod (orange), plane wave response created with `fdelmodc` (red), spherical wave response (blue) for a spatial window of (a) 5000 mm with no tapering, and Tukey apertures of (b) 500 mm, (c) 1000 mm, and (d) 1500 mm with a cosine fraction of 0.6.

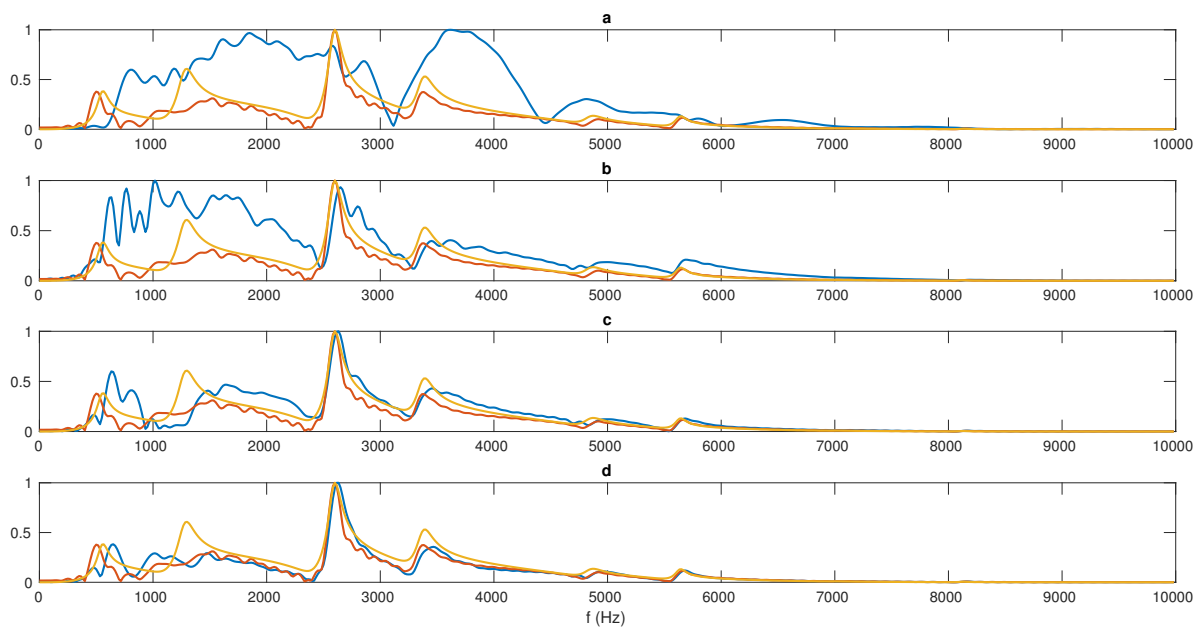


Figure 5.12: Normalized frequency responses for the elastic domain. sFWMod (orange), plane wave response created with `fdelmodc` (red), spherical wave response (blue) for a spatial window of (a) 5000 mm with no tapering, and Tukey apertures of (b) 500 mm, (c) 1000 mm, and (d) 1500 mm with a cosine fraction of 0.6.

6

Discussion, Recommendations, and Conclusions

This chapter encloses the discussion of the results, recommendation for further research and the conclusions. First, the modelling schemes are discussed. Next the sensitivity analysis, the proposed inversion method and multichannel measurements are considered. Lastly the conclusions are provided.

6.1. Discussion and Recommendation

6.1.1. Modelling

The (extended version of the) standing wave theory is not suitable for simulating and predicting the frequency response of a multilayered system. Therefore, `fdelmodc` is used and the `sFWMod` is created. Even though `fdelmodc` is primarily used for seismic wavefield modelling, scaling all parameters makes it applicable for any domain. However, the accuracy of the model is not validated for this use. Especially the absence of frequency peaks in the first 2000 Hz should be investigated. Furthermore, only vertical profile geometries are considered. The effect of non-symmetry, curved boundaries, artefacts, and velocity gradients need to be explored. It is possible to add attenuation in the EFD model. However, this is omitted due to an considerable increase in computation time and the preliminary nature of this study. Its effect on the measured spectra should be investigated.

6.1.2. Sensitivity analysis

A sensitivity analysis provides essential information about the usability of the IE method. Results show only layers with standing wave frequencies within the frequency band of the source wavelet can be imaged. Furthermore, IE is insensitive to small changes in reflection and transmission coefficients. A major limitation is the inability to measure the thickness and wave velocity individually. Prior information, when present, can be used to overcome this limitation. However, it should be accepted if this information is not available.

6.1.3. Inversion

It is impossible to create an inversion scheme based on one frequency peak due to its degenerate nature. Therefore, a scheme based on the peaks and troughs of the entire received frequency spectra is created. The IE method can only invert for layers with standing wave frequencies in the order of the source wavelet. The presented pre-processing steps are successfully implemented. They reduce the effect of the source wavelet and enhances the peaks and troughs positions. However, more research can be conducted to a different set. Currently, limited prior information is implemented in terms of an enclosed domain. More prior knowledge, if available, can be implemented by a linear or non-linear weight factor (Gennert and Yuille, 1988). This will accelerate the minimization finder as the gradients become larger. Prior information can be sourced from earlier measurements if time-lapse measurements are taken, or from other imaging methods. Additionally, noise can be added to the measured signal and the number of measurable layers can be increased to test its robustness.

The steepest descent method used in this study is a sufficient tool to find the global minima. However, there exist faster and more accurate algorithms. For instance, a combination between a brute force approach (where errors in a certain grid are calculated) and a minimum finder can be implemented. Other minimization algorithms like a conjugate gradient method can be implemented. However, this is challenging due to the non-linearity of the problem.

6.1.4. Multichannel measurements

Multichannel measurements are essential to map a spherical wave response to its plane wave equivalent. This makes it possible to use a fast forward model which simulates plane waves. Results show the importance of correctly suppressing reflections from the sides of the domain, especially in the elastic domains. Furthermore, tapering the aperture is essential to minimize simulation artefacts. An aperture width of 500 mm seems sufficient for both acoustic and elastic domains. However, these domains consist of vertical profiles geometrics only. Adding non-symmetry, curved boundaries, artefacts or a combination will change the way this model can be used. Furthermore, multichannel measurements were obtained with a spatial sampling size of 2 mm. This is impossible to achieve in a real measurement setup. Therefore, research to spatial sampling and additional signal processing methods should be conducted.

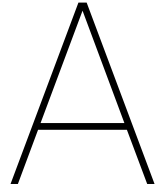
6.2. Conclusion

Traditional imaging techniques in medical ultrasound and seismic imaging require separation between received reflection events. When these event overlap in time, an imaging technique which uses the interference pattern in the frequency domain can be used. This method, called Impact Echo, has already been the standard for imaging concrete structures for decades. However, these usually consists of only one or two layers. This study introduces an inversion technique for multilayered domains.

Preliminary sensitivity analyses provide essential information about the usability of the Impact Echo method in combination with the proposed inversion strategy. Only layers with standing wave frequencies in the range of the source wavelet can be imaged. Layers with smaller travel times do not influence the performance of the method. Results show the inability to invert for thickness and wave velocity simultaneously. Only their ratio can be determined. Also, small variations in reflection and transmission coefficients do not alter its usability. Pre-processing steps are created to decrease the effect of the source wavelet. Moreover, these steps enhance the peaks and troughs position over their respective amplitude.

Multichannel measurements are necessary to transform a spherical wave response to its plane wave equivalent. This accelerates the inversion scheme as a computationally inexpensive forward model can be implemented. It is necessary to taper the signal at the edges of the receiver plane to minimize simulation artefacts. Summing over a aperture width of 500 mm seems enough to include the 1th Fresnel zone.

The proposed inversion scheme is tested on data of a simplified refractory wall. Here only vertical profile geometries are considered and no velocity gradients are implemented. The standing wave frequencies of the individual layers vary between 2 kHz and 375 kHz. Synthetic data is created with an Elastic Finite Difference method. A simplified Full Wavefield Modelling scheme is constructed and used as forward model. Here only plane wave responses are simulated. Results show the inversion scheme successfully inverts for three thicknesses in both acoustic and elastic domains.



Fourier Transform

The temporal Fourier transform is defined as

$$\hat{f}(\mathbf{r}, \omega) = \int_{-\infty}^{+\infty} dt f(\mathbf{r}, t) e^{-j\omega t}. \quad (\text{A.1})$$

The inverse Fourier transform is governed by

$$f(\mathbf{r}, t) = \frac{1}{2\pi} \int_{-\infty}^{+\infty} d\omega \hat{f}(\mathbf{r}, \omega) e^{j\omega t}. \quad (\text{A.2})$$

B

Derivation Angle-Dependent Transmission and Reflection Coefficients

Following (Brekhovskikh and Godin, 2012). Let the domain be in the x, z plane with a boundary at $z = 0$. The incoming wave travels in medium 1 where $z > 0$. Here the density ρ and wave velocity c are denoted with subscript 1. The second medium is situated at $z < 0$ with ρ_2 and c_2 . The incident plane wave arrives at the boundary with an angle θ_1 with respect to the z -axis. Using the solution of the Helmholtz equation as given in Eq. (2.7), the incidence pressure becomes

$$\hat{p}_{inc} = \hat{P}_0 e^{ik_1(x\sin\theta_1 - z\cos\theta_1)}. \quad (\text{B.1})$$

This wave is reflected. The reflected pressure becomes

$$\hat{p}_r = R\hat{P}_0 e^{ik_1(x\sin\theta_1 + z\cos\theta_1)}. \quad (\text{B.2})$$

The total pressure in medium 1 is the summation of these two pressures:

$$\hat{p}_1 = \hat{P}_0 e^{ik_1(x\sin\theta_1 - z\cos\theta_1)} + R\hat{P}_0 e^{ik_1(x\sin\theta_1 + z\cos\theta_1)}. \quad (\text{B.3})$$

The transmitted pressure becomes

$$\hat{p}_2 = \hat{p}_t = T\hat{P}_0 e^{ik_2(x\sin\theta_2 - z\cos\theta_2)}. \quad (\text{B.4})$$

Using $p = -\rho \frac{\delta \tilde{v}}{\delta t^2}$ with \tilde{v} being the velocity, we could do the same for the velocity. This results in

$$\tilde{v}_1 = -\frac{i\hat{P}_0}{\rho_1\omega} \left[e^{ik_1(x\sin\theta_1 - z\cos\theta_1)} + R e^{ik_1(x\sin\theta_1 + z\cos\theta_1)} \right], \quad (\text{B.5})$$

$$\tilde{v}_2 = \tilde{v}_t = -\frac{i\hat{P}_0}{\rho_2\omega} T e^{ik_2(x\sin\theta_2 - z\cos\theta_2)}. \quad (\text{B.6})$$

Applying the condition that at $z=0$ the pressure and parallel component of the velocity should be continuous, results in

$$\hat{P}_0 e^{ik_1(x\sin\theta_1)} + R\hat{P}_0 e^{ik_1(x\sin\theta_1)} = T\hat{P}_0 e^{ik_2(x\sin\theta_2)}, \quad -\infty < x < \infty, \quad (\text{B.7})$$

$$-\frac{i\hat{P}_0}{\rho_1\omega} \left[e^{ik_1(x\sin\theta_1)} + R e^{ik_1(x\sin\theta_1)} \right] = \tilde{v}_t = -\frac{i\hat{P}_0}{\rho_2\omega} T e^{ik_2(x\sin\theta_2)}, \quad -\infty < x < \infty. \quad (\text{B.8})$$

Eq. (B.7) results in

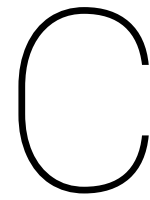
$$T = 1 + R, \quad (\text{B.9})$$

while Eq. (B.8) implies

$$1 - R = \frac{\rho_1 k_2 \cos(\theta_2)}{\rho_2 k_1 \cos(\theta_1)} T. \quad (\text{B.10})$$

From here R and T can be derived. These are

$$R = \frac{Z_2 \cos(\theta_1) - Z_1 \cos(\theta_2)}{Z_2 \cos(\theta_1) + Z_1 \cos(\theta_2)}, \quad T = \frac{2Z_2 \cos(\theta_1)}{Z_2 \cos(\theta_1) + Z_1 \cos(\theta_2)}. \quad (\text{B.11})$$



Kenneth Modelling

Kennett model (Kennett, 1979) for the furnace application. P_1^- is the wavefield at the refractory/air interface. Here the subscript i denotes the boundary, W_i is the propagation operator between boundary $i - 1$ and i .

D

Inversion Data

D.1. Varying frequency window

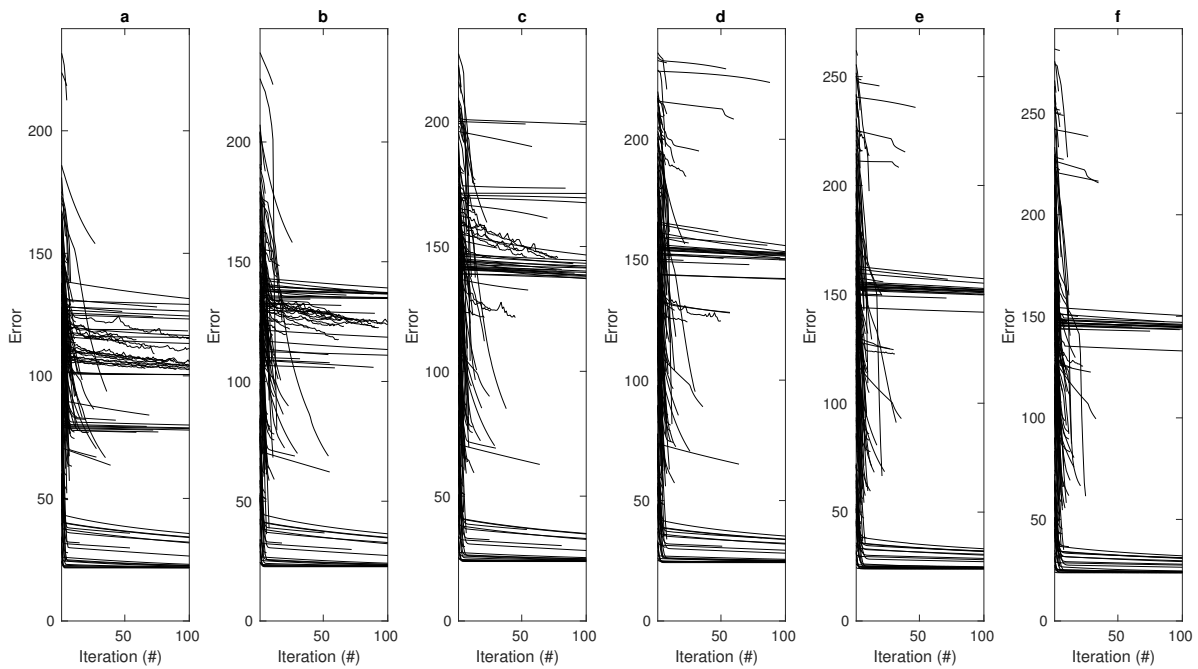


Figure D.1: Error plots for 200 parameter sets \mathbf{m} with varying frequency windows for calculating the moving mean of (a) 750 to (f) 2000 Hz.

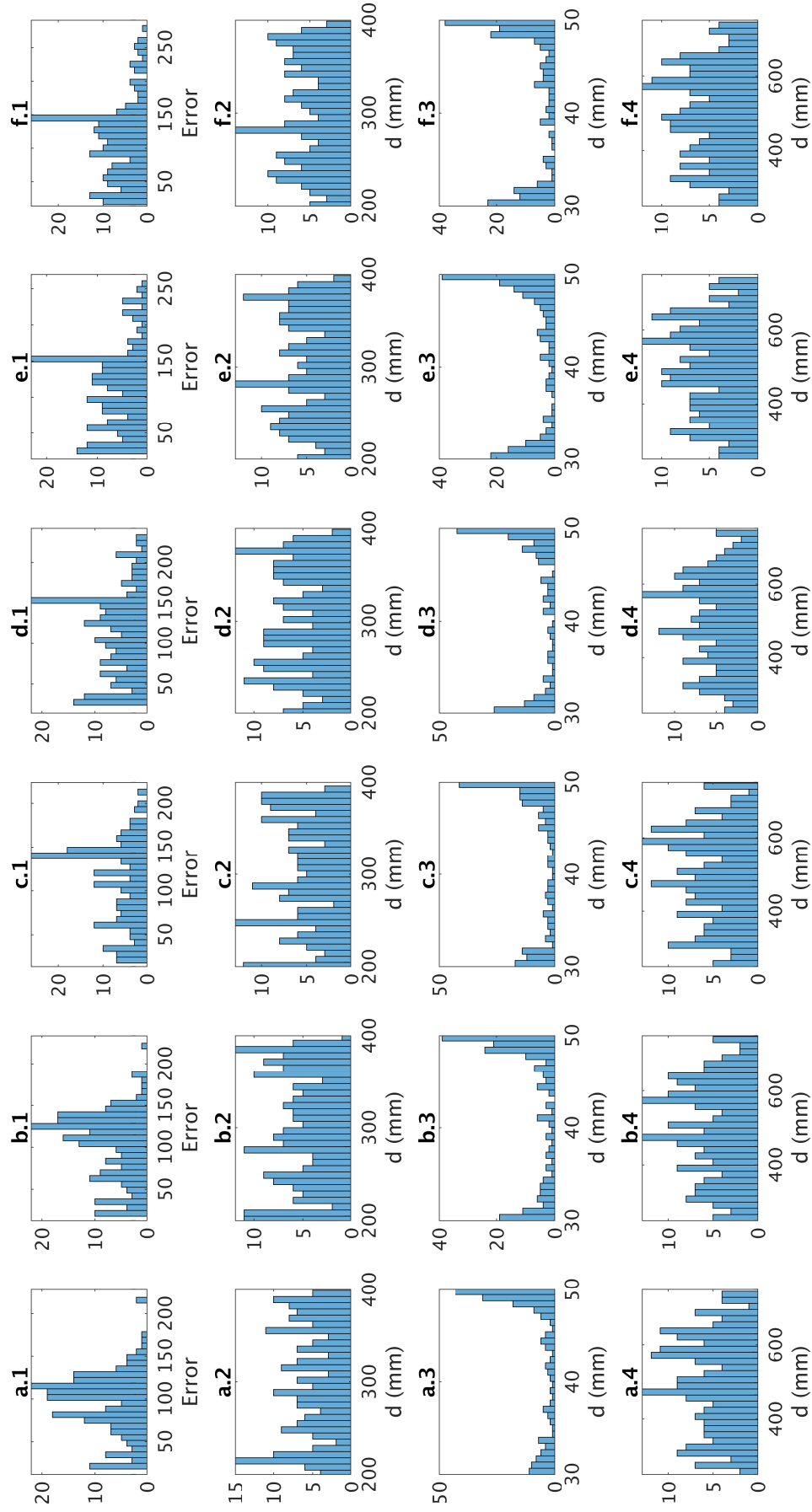


Figure D.2: Histograms for entire parameter set {m}. Different frequency windows for calculating the moving mean of (a) 750 to (f) 2000 Hz in increments of 250 Hz. x.1, x.2, x.3, x.4 show the histogram for the errors, and graphite, ramming, and semi-graphite layer thickness, respectively.

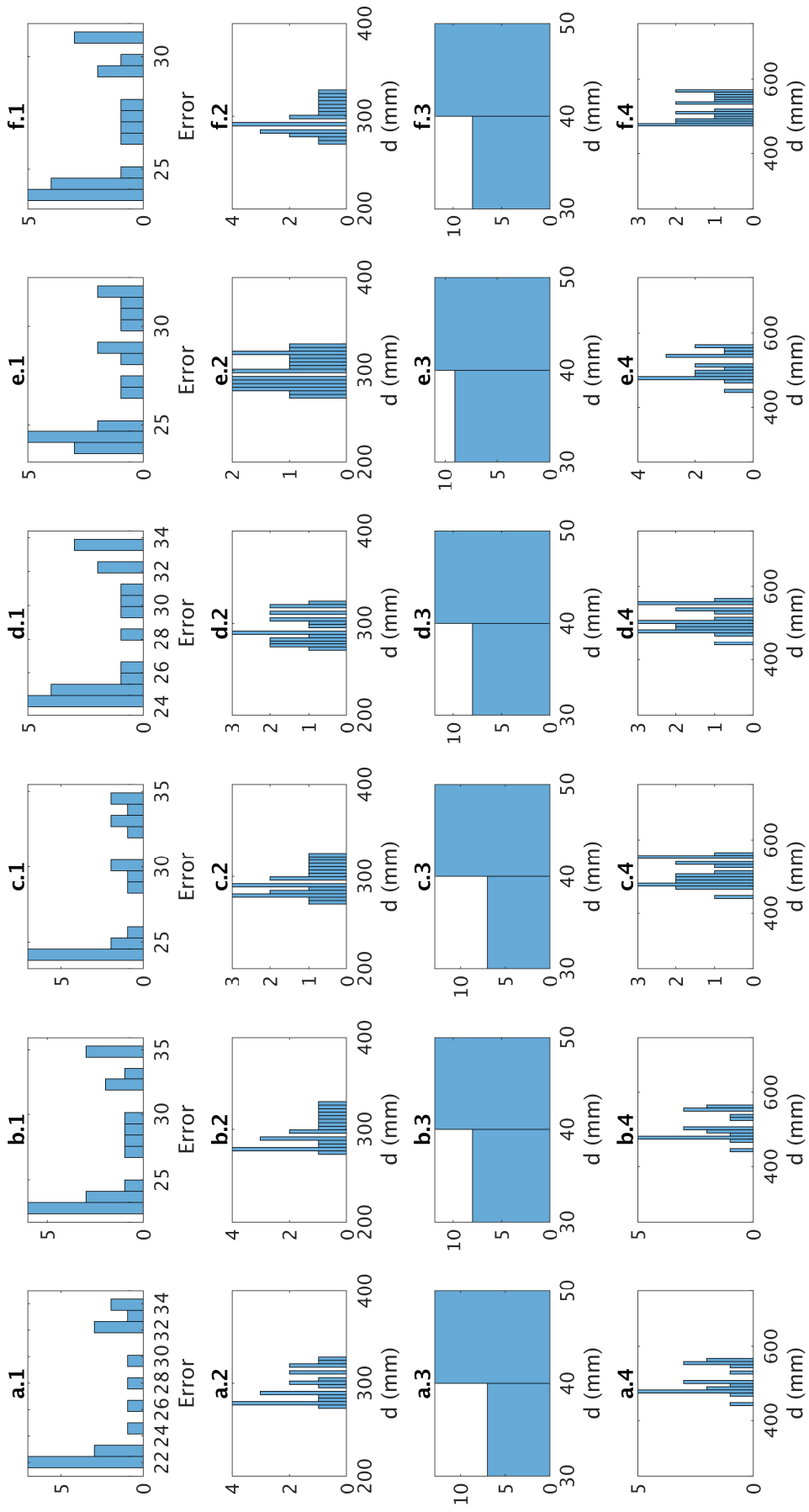


Figure D.3: Histograms for 50 parameter m with lowest error. Different frequency windows for calculating the moving mean of (a) 750 to (f) 2000 Hz in increments of 250 Hz. x.1, x.2, x.3, x.4 show the histogram for the errors, and graphite, ramming, and semi-graphite layer thickness, respectively.

D.2. Varying scaling factor

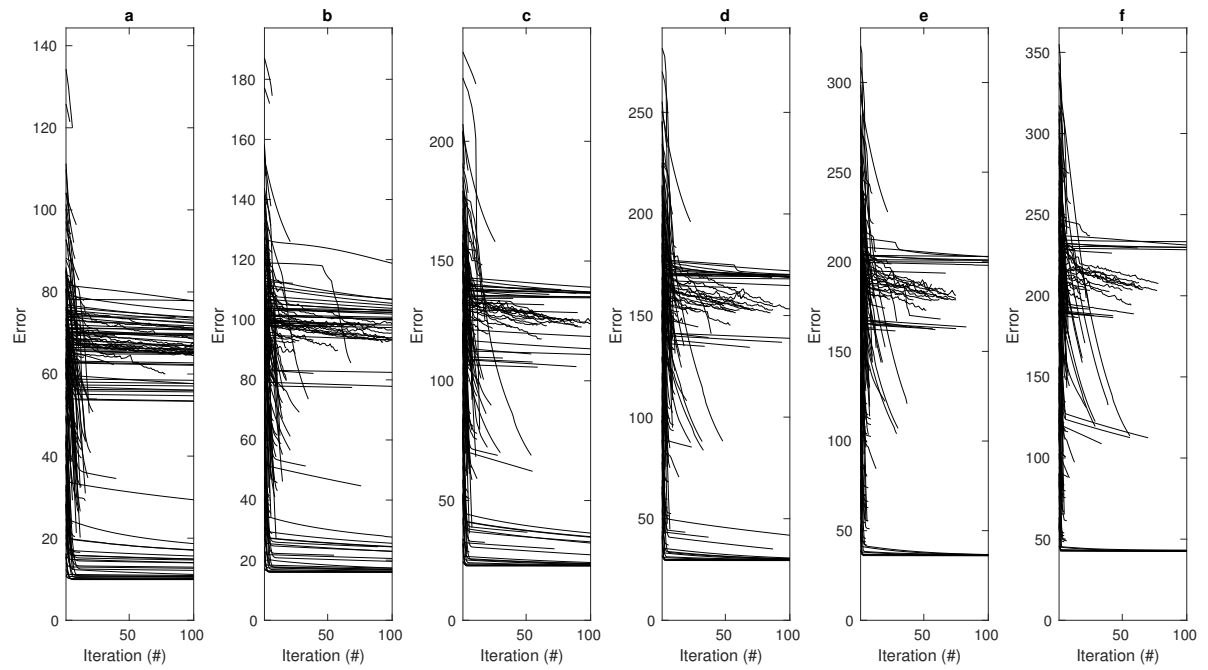


Figure D.4: Error plots for 200 parameter sets \mathbf{m} with varying compression functions with scaling factors γ of (a) 1 to (f) 6.

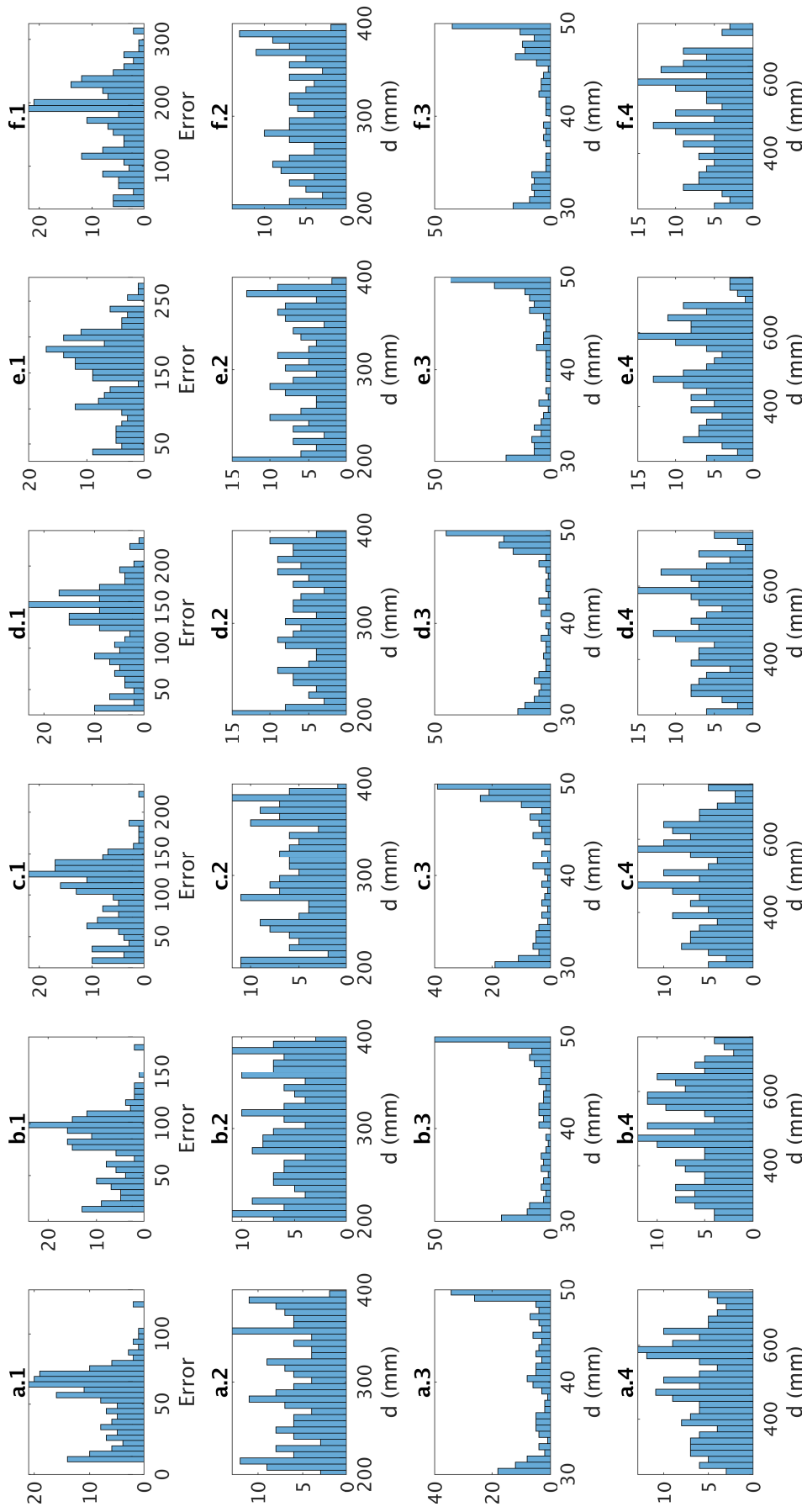


Figure D.5: Histograms for entire parameter set [m]. Different compression functions with scaling factors γ between (a) 1 to (f) 6 in increments of 1 Hz. x.1, x.2, x.3, x.4 show the histogram for the errors, and graphite, ramming, and semi-graphite layer thickness, respectively.

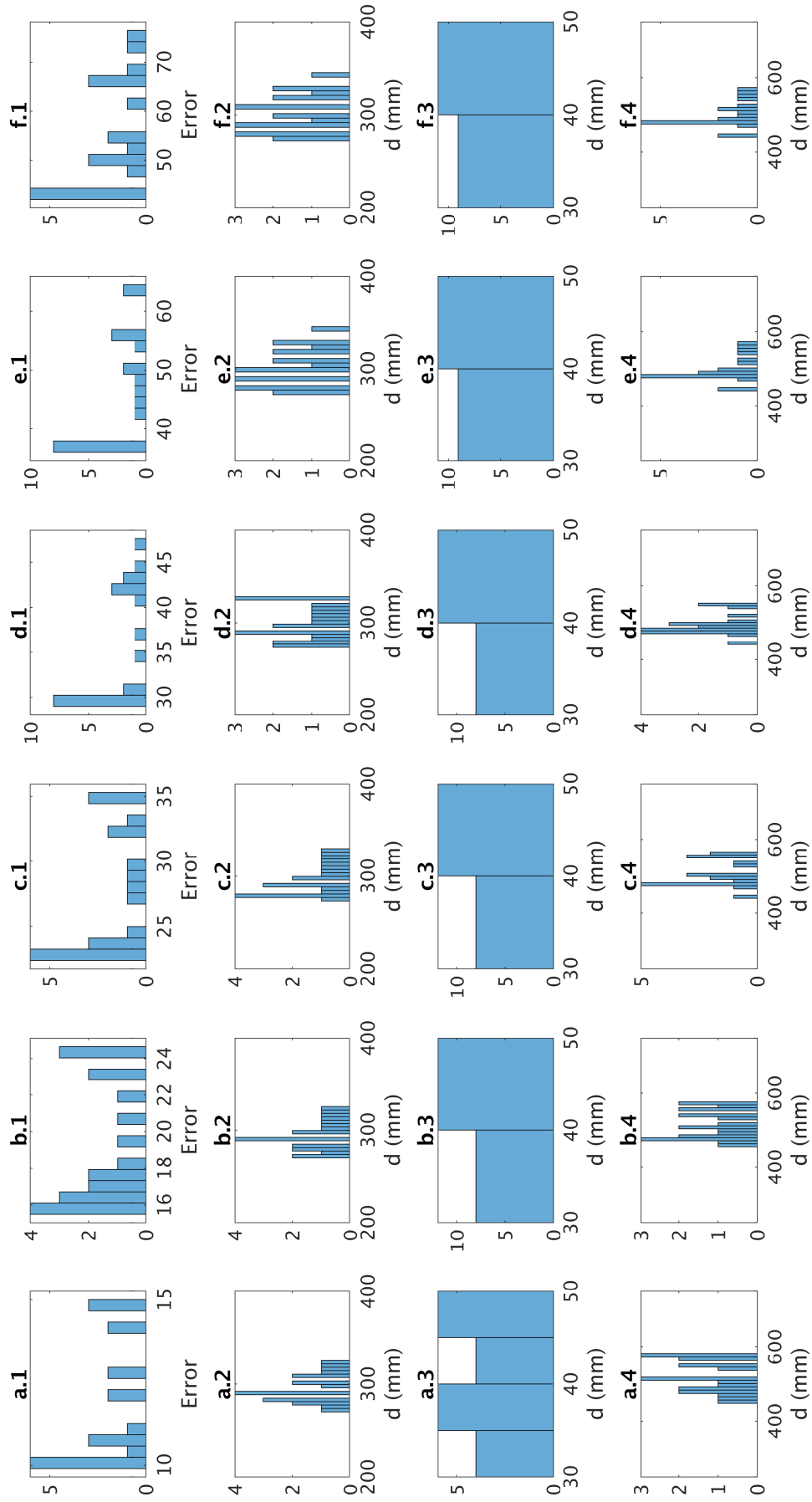


Figure D.6: Histograms for 50 parameter m with lowest error. Different compression functions with scaling factors γ between (a) 1 to (f) 6 in increments of 1 Hz. x.1, x.2, x.3, x.4 show the histogram for the errors, and graphite, ramming, and semi-graphite layer thickness, respectively.

Bibliography

- Aki, K. and Richards, P. G. (2002). *Quantitative seismology*.
- Alford, R., Kelly, K., and Boore, D. M. (1974). Accuracy of finite-difference modeling of the acoustic wave equation. *Geophysics*, 39(6):834–842.
- Bath, M. (2013). *Introduction to seismology*, volume 27. Birkhäuser.
- Berkhout, A. (1984). Multidimensional linearized inversion and seismic migration. *Geophysics*, 49(11):1881–1895.
- Berkhout, A. J. (1987). Applied seismic wave theory.
- Berkhout, A. J. (2012). *Seismic Migration: Imaging of Acoustic Energy by Wave Field Extrapolation...: Imaging of Acoustic Energy by Wave Field Extrapolation*. Elsevier.
- Bolf, N. (2004). Application of infrared thermography in chemical engineering. *Kemija u industriji/Journal of Chemists and Chemical Engineers*, 53:549–555.
- Brekhovskikh, L. M. and Godin, O. A. (2012). *Acoustics of layered media I: Plane and quasi-plane waves*, volume 5. Springer Science & Business Media.
- Bremmer, H. (1951). The wkb approximation as the first term of a geometric-optical series. *Communications on pure and applied mathematics*, 4(1):105–115.
- Courant, R., Friedrichs, K., and Lewy, H. (1967). On the partial difference equations of mathematical physics. *IBM journal of Research and Development*, 11(2):215–234.
- Cramér, H. and Grenander, U. (1959). *Probability and statistics: the Harald Cramér volume*. Almqvist & Wiksell.
- Fadugba, S., Edogbanya, O., and Zelibe, S. (2013). Crank nicolson method for solving parabolic partial differential equations. *IJA2M*, 1(3):8–23.
- Fornberg, B. (1988). Generation of finite difference formulas on arbitrarily spaced grids. *Mathematics of computation*, 51(184):699–706.
- Gennert, M. A. and Yuille, A. L. (1988). Determining the optimal weights in multiple objective function optimization. In *ICCV*, pages 87–89.
- Gisolf, D. and Verschuur, E. (2016). *The principles of quantitative acoustical imaging*. Eage Publications.
- John, B., Instruments, G., Lin, Y., Sansalone, M., Neville, A., Sansalone, M., Carino, N., Sansalone, M., Street, W., Sansalone, M., et al. (1982). Laboratory and field study of impact-echo method for flaw detection in concrete: Non-destructive testing of concrete. *Journal of Applied Sciences*, 2(9):pp–35.
- Kennett, B. (1979). Theoretical reflection seismograms for elastic media. *Geophysical Prospecting*, 27(2):301–321.
- Lindsey, J. (1989). The fresnel zone and its interpretive significance. *The Leading Edge*, 8(10):33–39.
- MATLAB (2018). *version 9.5.0 (R2018b)*. The MathWorks Inc., Natick, Massachusetts.
- Sadri, A., Gebiski, P., and Gordon, Y. (2014). Non-destructive testing (ndt) and inspection of the blast furnace refractory lining by stress wave propagation technique. *The creative heritage of BE Grum-Grzhimailo: history, current status, future. Part 1. — Yekaterinburg, 2014*.

- Sadri, A., Gebski, P., Mirkhani, K., and McGarrie, G. (2009). New and innovative non-destructive testing (ndt) techniques for inspection and monitoring of metal smelting furnaces. In *NDT in Canada 2009, Conference and the 6th International Workshop: Advances in Signal Processing for Non Destructive Evaluation of the Materials*.
- Sadri, A., Ying, W., Gebski, P., Szyplinski, P., Goff, T., and van Beek, B. (2015). A comprehensive review of acousto ultrasonic-echo (au-e) technique for furnace refractory lining assessment. In *54th annual conference of metallurgists, COM*.
- Scott, A. (2006). *Encyclopedia of nonlinear science*. Routledge.
- Sei, A. (1995). A family of numerical schemes for the computation of elastic waves. *SIAM Journal on Scientific Computing*, 16(4):898–916.
- Sharp, C., Gordon, Y., Liu, S., Towsey, P., Cameron, I., et al. (2012). Impact of cokemaking technology on a steel plant's carbon footprint. In *Carbon Management Technology Conference*. Carbon Management Technology Conference.
- Sheriff, R. (1985). Aspects of seismic resolution: Chapter 1.
- Sheriff, R. E. (1996). Understanding the fresnel zone. *AAPG Explorer*, pages 18–19.
- Theocaris, P. and Prassianakis, J. (1974). The mohr envelope of failure for concrete: a study of its tension-compression part. *Magazine of Concrete Research*, 26(87):73–82.
- Thorbecke, J. (1993). Makewave. <https://github.com/JanThorbecke/OpenSource/tree/master/fdelmodc>.
- Thorbecke, J. W. and Draganov, D. (2011). Finite-difference modeling experiments for seismic interferometry. *Geophysics*, 76(6):H1–H18.
- Varghese, B., DeConick, C., Cartee, G., Zoughi, R., Velez, M., and Moore, R. (2005). High-temperature monitoring of refractory wall recession using frequency-modulated continuous-wave (fm-cw) radar techniques. In *AIP Conference Proceedings*, volume 760, pages 1714–1720. AIP.
- Virieux, J. (1986). P-sv wave propagation in heterogeneous media: Velocity-stress finite-difference method. *Geophysics*, 51(4):889–901.
- Virieux, J. and Operto, S. (2009). An overview of full-waveform inversion in exploration geophysics. *Geophysics*, 74(6):WCC1–WCC26.
- Wang, C.-Y., Chiu, C.-L., Tsai, K.-Y., Chen, P.-K., Peng, P.-C., and Wang, H.-L. (2014). Inspecting the current thickness of a refractory wall inside an operational blast furnace using the impact echo method. *NDT & E International*, 66:43–51.
- Wirgin, A. (2004). The inverse crime. *arXiv preprint math-ph/0401050*.

Acknowledgements

I would love to close this thesis with some special thanks to the people who supported me.

First and foremost Dr. Eric Verschuur and Dr. Koen van Dongen for the daily supervision. Our meetings were fruitful, always flew by and helped me put together a complete thesis. You showed me to first take a step back before diving into the problem at hand.

Koen, I'm grateful for your personal support. Your compassion and connection with students and your ability of teaching is a gift.

Gerard Louwerse, Joost Storm, and Colin Commandeur of TATA Steel. Our meetings were a good reality check and showed the connection between my education and industry. I really enjoyed the tour of the blast furnace which is a once in a lifetime opportunity.

Special thanks to Prof. Nico de Jong, Dr. Aurele Adam, Eric, and Gerard for being in my committee.

My gratitude to everybody in the AWI-room, especially Thijs and Rick. We not only shared some of our physics problems, but also the muffins and fish on Thursdays. The (small) breaks playing Babyfoot were a good opportunity to relax and for me to boost your self-esteem (yes I let you win most of the time).

Best,
Adriaan

